SIN-3 transcriptional coregulator maintains mitochondrial homeostasis and polyamine flux

Marina Giovannetti, Maria-Jesus Rodriguez-Palero, Paola Fabrizio, Ophélie Nicolle, Cécile Bedet, Grégoire Michaux, Michael Witting, Marta Artal-Sanz, Francesca Palladino

To cite this version:

Marina Giovannetti, Maria-Jesus Rodriguez-Palero, Paola Fabrizio, Ophélie Nicolle, Cécile Bedet, et al.. SIN-3 transcriptional coregulator maintains mitochondrial homeostasis and polyamine flux. iScience, 2024, 27 (5), pp.109789. ⟨10.1016/j.isci.2024.109789⟩. ⟨hal-04615761⟩

HAL Id: hal-04615761
https://hal.science/hal-04615761v1

Submitted on 5 Sep 2024

iScience

CellPress
OPEN ACCESS

Article

SIN-3 transcriptional coregulator maintains mitochondrial homeostasis and polyamine flux

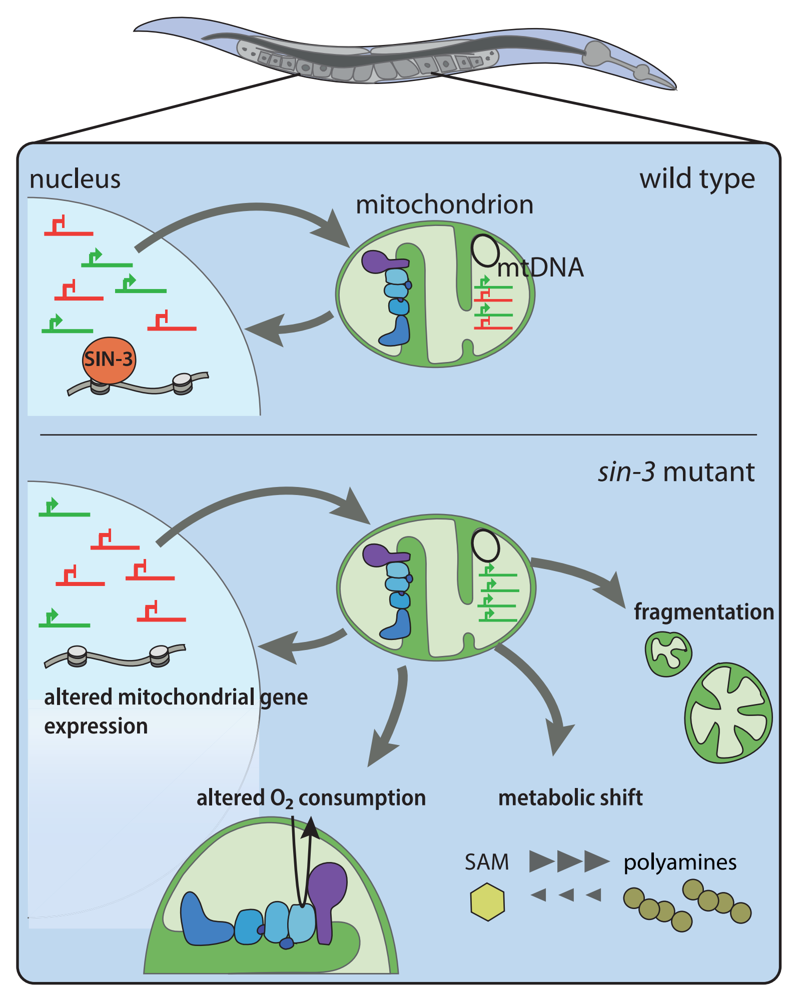

Marina Giovannetti, María-Jesús Rodríguez-Palero, Paola Fabrizio, ..., Michael Witting, Marta Artal-Sanz, Francesca Palladino

martsan@upo.es (M.A.-S.)
francesca.palladino@ens-lyon.fr (F.P.)

Highlights

Loss of SIN-3 coregulator causes transcriptional deregulation of mitochondrial genes

C. elegans sin-3 mutants show mitochondrial fragmentation and altered respiration

Sin-3 mutants also display reduced levels of SAM and accumulation of polyamines

Giovannetti et al., iScience *27*, 109789
May 17, 2024
https://doi.org/10.1016/j.isci.2024.109789

iScience

CellPress OPEN ACCESS

Article

SIN-3 transcriptional coregulator maintains mitochondrial homeostasis and polyamine flux

Marina Giovannetti,[1,6,7] María-Jesús Rodríguez-Palero,[2,6] Paola Fabrizio,[1] Ophélie Nicolle,[3] Cécile Bedet,[1] Grégoire Michaux,[3] Michael Witting,[4,5] Marta Artal-Sanz,[2,*] and Francesca Palladino[1,8,*]

SUMMARY

Mitochondrial function relies on the coordinated transcription of mitochondrial and nuclear genomes to assemble respiratory chain complexes. Across species, the SIN3 coregulator influences mitochondrial functions, but how its loss impacts mitochondrial homeostasis and metabolism in the context of a whole organism is unknown. Exploring this link is important because *SIN3* haploinsufficiency causes intellectual disability/autism syndromes and SIN3 plays a role in tumor biology. Here we show that loss of *C. elegans* SIN-3 results in transcriptional deregulation of mitochondrial- and nuclear-encoded mitochondrial genes, potentially leading to mito-nuclear imbalance. Consistent with impaired mitochondrial function, *sin-3* mutants show extensive mitochondrial fragmentation by transmission electron microscopy (TEM) and *in vivo* imaging, and altered oxygen consumption. Metabolomic analysis of *sin-3* mutant animals revealed a mitochondria stress signature and deregulation of methionine flux, resulting in decreased S-adenosyl methionine (SAM) and increased polyamine levels. Our results identify SIN3 as a key regulator of mitochondrial dynamics and metabolic flux, with important implications for human pathologies.

INTRODUCTION

Mitochondria, the main energy providers within cells, produce ATP through oxidative phosphorylation (OXPHOS) and control the levels of many metabolites essential for various cellular functions. The OXPHOS system consists of four multimeric complexes, coenzyme Q and cytochrome *c* that form the mitochondrial respiratory chain (I–IV) and couple redox reactions, creating an electrochemical gradient leading to the creation of ATP through a fifth complex, the F_1F_0 ATPase.[1] Assembly of functional mitochondria relies on coordinated transcription and translation of mitochondrial and nuclear genomes,[2] and both mitochondrial and nuclear DNA mutations affecting the accumulation and function of OXPHOS enzymes are the most common cause of mitochondrial diseases and are associated with neurodegeneration and aging.[3–5] The mitochondrial genome, which is highly conserved among species, comprises 37 genes coding for two ribosomal RNAs, 22 transfer RNAs, and 13 protein subunits (12 for *C. elegans*) of the mitochondrial respiratory chain performing OXPHOS.[6] The rest of the mitochondrial proteome, comprising over a thousand proteins, is encoded in the nucleus.[7–9] The bidirectional regulation between mitochondria and the nucleus, referred to as mito-nuclear communication, maintains homeostasis and regulates stress responses.[10] Mitochondrial damage or alterations in mitochondrial function trigger specific quality control mechanisms. Of these, the best characterized is the mitochondrial unfolded protein response (UPR^{mt}), a cellular stress response that leads to increased transcription of mitochondrial chaperones and proteases.[11] In addition to an imbalance between mitochondrial and nuclear protein quantities,[12] reduced levels of TCA cycle components,[13] reduction of β-oxidation and lipid biosynthesis[14,15] and defective mitochondrial import,[16] can all trigger UPR^{mt}. Recent data have shown that mitochondrial stress leads to extensive chromatin reorganization,[17,18] and chromatin regulatory factors contribute to mitochondrial gene expression.[12] Conversely, metabolites originating from the mitochondria can initiate modifications in the nucleus.[12]

Depletion experiments in various models have shown that the highly conserved SIN3/HDAC coregulator plays a role in mitochondrial functions and metabolism.[19] Yeast *sin3* null mutants grow poorly on non-fermentable carbon sources, have lower ATP levels, and reduced

---

[1] Laboratory of Biology and Modeling of the Cell, UMR5239 CNRS/Ecole Normale Supérieure de Lyon, INSERM U1210, UMS 3444 Biosciences Lyon Gerland, Université de Lyon, Lyon, France
[2] Andalusian Centre for Developmental Biology (CABD), Consejo Superior de Investigaciones Científicas/Junta de Andalucía/Universidad Pablo de Olavide and Department of Molecular Biology and Biochemical Engineering, Universidad Pablo de Olavide, 41013 Sevilla, Spain
[3] University Rennes, CNRS, IGDR (Institut de Génétique et Développement de Rennes), UMR 6290, 35000 Rennes, France
[4] Metabolomics and Proteomics Core, Helmholtz Zentrum München, Ingolstädter Landstraße 1, 85764 Neuherberg, Germany
[5] Chair of Analytical Food Chemistry, TUM School of Life Sciences, Technical University of Munich, Maximus-von-Imhof Forum 2, 85354 Freising, Weihenstephan, Germany
[6] These authors contributed equally
[7] Present address: Université Paris Cité, CNRS, Institut Jacques Monod, 75013 Paris, France
[8] Lead contact
*Correspondence: martsan@upo.es (M.A.-S.), francesca.palladino@ens-lyon.fr (F.P.)

https://doi.org/10.1016/j.isci.2024.109789

respiration rates.[20] In *Drosophila* cultured cells, reduction of SIN3 levels also resulted in altered ATP levels and deregulation of genes encoded by the mitochondrial genome.[20,21] Lower levels of ATP and increased sensitivity to oxidative stress were also observed in *C. elegans* animals carrying the *sin-3(tm1276)* partial loss of function allele.[22] In mice, Sin3a was detected in a transcriptional complex with the MafA pancreatic β cell-specific activator,[23] and its inactivation reduced the fitness of β cells and altered glucose production in the liver.[24] Significantly, in mammalian cells, SIN3 and its associated protein SUDS3 were identified in a screen for modifiers of drug-induced mitochondrial dysfunction.[25] Altogether, these data from different systems support a conserved role for SIN3 in mitochondrial homeostasis and metabolism, but how SIN3 affects mitochondrial dynamics and metabolic pathways in the context of a whole organism remains largely unknown. This is particularly important given that heterozygous loss-of-function variants, as well as point mutations in *SIN3* were recently identified as the underlying cause of intellectual disability (ID)/autism syndromes,[26–28] and SIN3 levels play an important role in tumor biology.[29–32]

Previous studies in *C. elegans* have shown that knockdown of *sin-3*, the single SIN3 homolog in this organism, results in a decreased lifespan, altered mitochondrial membrane potential, enhanced autophagy and increased oxidative stress.[22,33] How these changes affect mitochondrial morphology and function was not investigated. Here, using a *sin-3* CRISPR-Cas9 knock-out allele, we show that loss of SIN-3 results in the deregulation of both mitochondria- and nuclear-encoded genes. Transmission electron microscopy (TEM) and *in vivo* imaging revealed extensive fragmentation of mitochondria in all tissues examined, including muscle, intestine, hypodermis, and the germline. Consistent with severe defects in mitochondrial function, both basal and maximal oxygen consumption are increased in the absence of SIN3, while spare respiratory capacity is decreased. Metabolomic analysis identified a signature of mitochondria stress and deregulation of methionine flux, resulting in reduced levels of SAM and a shift toward higher polyamine levels. Together our data identify SIN3 as an important regulator of mitochondrial dynamics in an organismal context, and reveal a SIN-3- dependent connection between expression of OXPHOS subunits, mitochondrial homeostasis, and metabolic fluxes.

RESULTS

Loss of *sin-3* results in altered expression of genes with mitochondrial functions

Previous transcriptomic analysis in young adults carrying the *sin-3(tm1276)* partial loss-of-function mutation revealed deregulation of the germline transcriptome, including metabolic genes.[34] In order to identify high-confidence genes regulated by SIN-3, we extended our analysis to genes commonly misregulated in *sin-3(tm1276)* and *sin-3(syb2172)* young adults that carry a complete loss of function allele obtained by CRISPR-Cas9,[34] generating a list of 892 genes (Table S1). Using Worm Cat,[35] within this set we identified a common class of genes with functions related to mitochondria (Figure 1A; Table 1).

Both nuclear- and mitochondrial-encoded genes contribute to the assembly of mitochondrial respiratory chain complexes (MRC) I-V.[1] Five of the 7 MRC complex I subunits encoded by the mitochondrial genome were strongly upregulated in both *sin-3* mutants: *ndub-2*, *ndfl-4*, *nduo-1*, *nduo*-2, and *nduo-5* (Figure 1B). By contrast, nuclear-encoded MRC subunits identified in our dataset were mostly downregulated (Figure 1B), as were the majority of additional nuclear-encoded genes with mitochondria-related functions (31 out of 37, Table 1). These include mitochondrial ribosomal proteins, components of the citric acid cycle, the *tomm-40* translocase and the *coq-3* coenzyme Q3. Comparison of our list of misregulated genes associated with mitochondrial functions to a list of SIN3 targets on chromatin[36] revealed that 23 of these 37 genes have SIN-3 binding at their promoter region, and the majority (18/23) are downregulated in *sin-3* mutants, including ribosomal protein genes, the t*omm-40* mitochondrial translocase, the ATP synthases *atp-1* and *atp-4*, and the cytochrome *c* oxidase *cox-7C* (Table S2). SIN-3 may therefore directly promote expression of these genes. Together, our analyses suggest that loss of *sin-3* perturbs the coordinated expression of mitochondrial genes encoded by nuclear and mitochondrial genomes, possibly resulting in mito-nuclear imbalance and affecting mitochondrial homeostasis. Consistent with mitochondrial dysfunction, *sin-3* mutants show reduced fertility, increased sensitivity to oxidative stress[22,33,34,36] and altered lifespan[22,33] (Figure S1), as observed in other mitochondrial mutants.[37]

Transmission electron microscopy reveals extensive mitochondrial fragmentation in *sin-3* mutant animals in all tissues examined

Mitochondrial morphology is tightly linked to mitochondrial function, and its steady state is determined by the balance between fission and fusion events that may be disrupted under conditions of mitochondrial stress.[38] To test whether mitochondrial morphology is affected in *sin-3* mutant animals we performed electron microscopy analyses on wild type and mutant young adults. Mitochondria in the body wall muscles of wild type animals vary in size reflecting dynamic morphological changes, and tend to be cylindrical- or ovular-shaped with regular outer membranes and dense cristae throughout each organelle (Figure 2 panel *a*, white arrows). In animals carrying the loss of function allele *sin-3(tm1276)*, or the *sin-3(syb2172)* null allele, mitochondria were instead highly fragmented and appeared more numerous, with a stronger effect in *syb2172* animals (Figure 2 panels *b* and *c,* white arrows). For both mutants, highly fragmented mitochondria were visible in all of the tissues examined, including intestine, pharynx, hypodermis, and germline (Figures 2A and S2A). We also observed the presence of enlarged or "giant" mitochondria, most prominent in muscle and intestinal cells, and often containing electron-dense material (Figure 2A panels *b*, *c*, and *e*; Figure 2B panels *a-d,* black arrows) that may indicate iron deposits[39–41] or protein aggregates.[42–45] Mitochondria morphology is most easily studied in muscle cells on the outer body surface: these are relatively large and flat, making it possible to easily evaluate mitochondria size, shape, and distribution.[46] Our analysis revealed that for both mutants, the perimeter and surface area of individual mitochondria in these cells decreased, and the effect was greater for the *sin-3(syb2172)* allele (Figures 2C and S2B). We also observed an increase in the average circularity index, although this was only statistically significant for the *sin-3(syb2172)* null allele (Figure 2C), and an increase in the number of individual mitochondria (Figure S2C). These findings suggest that loss of SIN-3 decreases mitochondrial fusion and increases fission events.

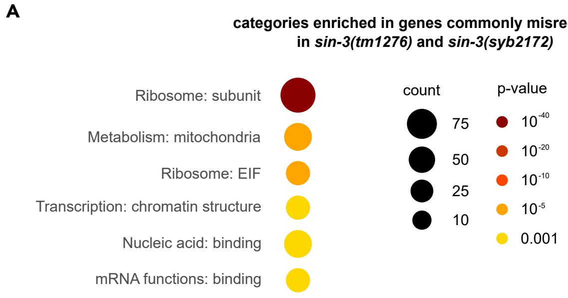

B

mitochondrial complex	subunit identity	mammalian homologue	misregulation in *sin-3*
complex I	***ndub-2***	NDUFB2	UP
	ndfl-4	NADH dehydrogenase	UP
	nduo-1	MT-ND1	UP
	nduo-2	NADH dehydrogenase	UP
	nduo-5	MT-ND5	UP
	Y54F10AM.5	NDUFA8	UP
complex III	***ucr-2.1***	UQCRC2	UP
	ucr-2.3	UQCRC2	DOWN
	cyc-2.1	CYCS	DOWN
complex IV	*cox-7C*	COX7C	DOWN
complex V	*atp-1*	ATP5F1A	DOWN
	R53.4	ATP5MF	DOWN
	atp-4	ATP5PF	DOWN
	Y82E9BR.3	ATP5MC1	DOWN

Figure 1. Loss of *sin-3* alters the expression of mitochondrial genes

(A) WormCat visualization of categories enriched in genes commonly misregulated in *sin-3(tm1276)* and *sin-3(syb2172)* mutants at the young adult stage[34] (Table S1). The legend for bubble charts is indicated on the right, with size referring to the number of genes in each category and color referring to the *p* value.
(B) Respiratory complex subunits commonly misregulated in *sin-3(tm1276)* and *sin-3(syb2172)* mutants are indicated, along with their mammalian counterparts. Subunits encoded by the mitochondrial genome are shown in bold.

Time-dependent increase in mitochondrial fragmentation in *sin-3* muscle cells

To further examine mitochondria dynamics in live animals, we used a transgenic strain expressing a red fluorescent protein (RFP) fused at the N terminus to the TOMM-20 translocase of the outer mitochondrial membrane and expressed under the control of a promoter in muscle cells (*myo-3p::20Nter::*wrmScarlet)[47], where mitochondria are abundant and easily visible. We used *tm1276* mutant animals because although less fertile than wild type, they can be maintained as homozygotes, while *syb2172* animals are fully sterile.[34] In wild type, the majority of body-wall muscle cells have longitudinally arrayed tubular mitochondria, while a smaller percentage show either elongated mitochondria in an interconnected mesh-like network or fragmented mitochondria (Figure 3A). We arbitrarily classified mitochondrial morphology into three classes-tubular, intermediate, or fragmented,[48,49] and scored animals falling into each of these at days 1, 6, and 9 of adulthood. In wild-type day 1 adults, the large majority of mitochondria showed a tubular morphology (Figure 3B). Mitochondria of *sin-3(tm1276)* mutants of the same age were smaller and rounder compared to wild type, consistent with increased fragmentation and TEM results. At day 6, intermediate and fragmented mitochondria also appeared in wild type, when the majority of mitochondria in *sin-3* mutants were highly fragmented. At day 9, mitochondrial fragmentation further increased in *sin-3(tm1276)* mutants, but remained more or less constant in wild type (Figure 3B). As an independent measure of mitochondrial morphology we used ImageJ software analysis (Figure 3C). In agreement with the TEM results, we observed a decrease in the average perimeter and surface area of individual mitochondria in *sin-3* mutants, and an increase in roundness (Figure 3C).[50,51] Using a *mex-5p*::tomm-20:mKate2 reporter expressed in the germline, we also observed changes in mitochondrial morphology in this tissue (Figure S2D). Excessive mitochondrial fragmentation results from an imbalance between fusion and fission that are mediated primarily by two classes of GTPases structurally related to dynamins: mitofusins (MFNs)/Fzo1/FZO-1 and Drp1/DRP-1, respectively.[38,46,52] Expression of neither gene was altered in *sin-3* mutants[34] (Table S1). Because of the absence of *C. elegans* specific antibodies, we were unable to look at protein levels of mitofusin or DRP-1 proteins.

To measure whether mitochondrial mass increases in *sin-3(tm1276)* mutants we used MitoTracker Green (MTG), a widely used fluorescence dye that accumulates in mitochondria independent of mitochondrial membrane potential.[44] MTG staining was significantly increased in day 6 mutant animals (Figure 3D, left panel). Increased staining in mutant animals was also observed using the membrane potential sensitive dye tetramethylrhodamine, ethyl ester (TMRE) that accumulates in active mitochondria[44] (Figure 3D, right panel). Together, these results suggest that loss of SIN-3 leads to an increase in total mitochondrial mass, as suggested by TEM results in young adults.

Table 1. List of genes with mitochondrial function commonly misregulated in both *sin-3(syb2172)* and *sin-3(tm1276)* germlines from young adults

WB_ID	sequence_ID	category	misregulation
WBGene00010042	*bcs-1*	Metabolism: mitochondria: chaperone	DOWN
WBGene00016442	C35D10.5	Metabolism: mitochondria: chaperone	DOWN
WBGene00009139	F25H9.7	Metabolism: mitochondria: citric acid cycle	DOWN
WBGene00010317	*idh-1*	Metabolism: mitochondria: citric acid cycle	DOWN
WBGene00016844	*sucg-1*	Metabolism: mitochondria: citric acid cycle	DOWN
WBGene00017759	*mrps-18B*	Metabolism: mitochondria: citric acid cycle	DOWN
WBGene00009712	***ndub-2***	**Metabolism: mitochondria: complex I**	**UP**
WBGene00010958	***ndfl-4***	**Metabolism: mitochondria: complex I**	**UP**
WBGene00010959	***nduo-1***	**Metabolism: mitochondria: complex I**	**UP**
WBGene00010961	***nduo-2***	**Metabolism: mitochondria: complex I**	**UP**
WBGene00010967	***nduo-5***	**Metabolism: mitochondria: complex I**	**UP**
WBGene00021849	*ndua-8*	Metabolism: mitochondria: complex I	UP
WBGene00012158	*ucr-2.1*	Metabolism: mitochondria: complex III	UP
WBGene00017121	*cyc-2.1*	Metabolism: mitochondria: complex III	DOWN
WBGene00020757	*ucr-2.3*	Metabolism: mitochondria: complex III	DOWN
WBGene00009161	*cox-7C*	Metabolism: mitochondria: complex IV	DOWN
WBGene00010419	*atp-1*	Metabolism: mitochondria: complex V	DOWN
WBGene00011273	R53.4	Metabolism: mitochondria: complex V	DOWN
WBGene00020275	*atp-4*	Metabolism: mitochondria: complex V	DOWN
WBGene00022336	Y82E9BR.3	Metabolism: mitochondria: complex V	DOWN
WBGene00001425	*fis-2*	Metabolism: mitochondria: morphology	UP
WBGene00022159	*mppa-1*	Metabolism: mitochondria: protease	UP
WBGene00007712	*mrpl-34*	Metabolism: mitochondria: ribosome	DOWN
WBGene00011759	*mrps-18B*	Metabolism: mitochondria: ribosome	DOWN
WBGene00011883	*mrpl-50*	Metabolism: mitochondria: ribosome	DOWN
WBGene00012992	*mrpl-20*	Metabolism: mitochondria: ribosome	DOWN
WBGene00018961	*mrps-16*	Metabolism: mitochondria: ribosome	DOWN
WBGene00020499	*mrps-18.C*	Metabolism: mitochondria: ribosome	DOWN
WBGene00020625	*mrrf-1*	Metabolism: mitochondria: ribosome	DOWN
WBGene00021350	Y37E3.8	Metabolism: mitochondria: ribosome	DOWN
WBGene00009305	*metl-17*	Metabolism: mitochondria: RNA methyltransferase	DOWN
WBGene00007686	*tomm-40*	Metabolism: mitochondria: translocase	DOWN
WBGene00013462	*micu-1*	Metabolism: mitochondria: transporter	DOWN
WBGene00000763	*coq-3*	Metabolism: mitochondria: ubiquinone	DOWN
WBGene00003967	*pdr-1*	Metabolism: mitochondria: unassigned	DOWN
WBGene00009187	F27D4.1	Metabolism: mitochondria: unassigned	DOWN
WBGene00011527	*cchl-1*	Metabolism: mitochondria: unassigned	DOWN
WBGene00014176	ZK1010.2	Metabolism: mitochondria: unassigned	DOWN
WBGene00020511	*immt-1*	Metabolism: mitochondria: unassigned	UP
WBGene00077500	C27H6.9	Metabolism: mitochondria: unassigned	DOWN

The list of all commonly misregulated genes was generated by crossing the set of genes obtained for each allele with an FDR <0.05 following DESeq2 analysis (Table S1), and the list of mitochondrial genes extracted from WormCat.[35] Genes encoded by the mitochondrial genome are shown in bold. See also Tables S1 and S2.

Muscle fibers degenerate prematurely in *sin-3* mutants

Mitochondrial dysfunction impairs muscle health and causes subsequent muscle wasting, commonly referred to as sarcopenia.[53] Using a muscle myosin reporter *myo-3*::GFP[54] in wild type young adults sarcomeres appear as straight lines of GFP, and no obvious change was observed up to day 9 (Figure 3E). By contrast, in *sin-3(tm 1276)* mutants at day 9 we observed diffuse GFP fluorescence, suggesting that muscle integrity

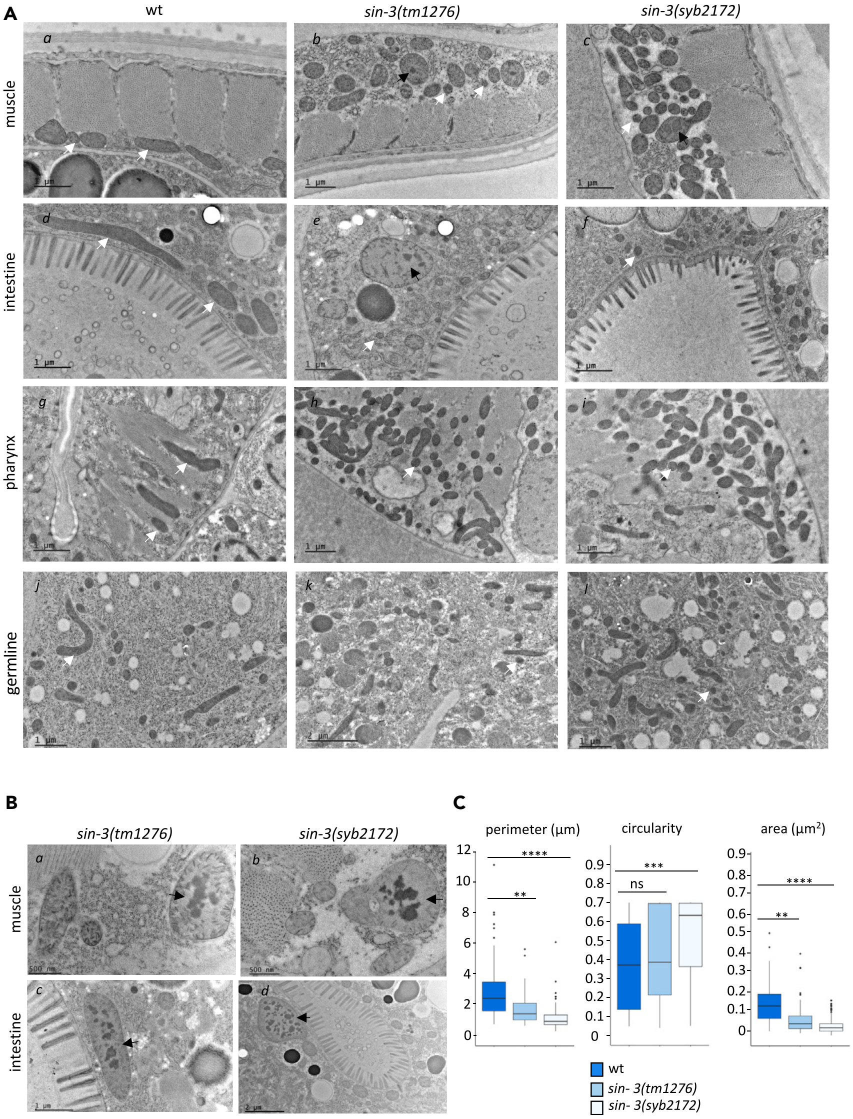

Figure 2. TEM microscopy of mitochondria in *sin-3* mutant animals

(A) Transverse sections captured with electron microscopy of mitochondria from the body wall muscles, intestine, pharynx and germline of young adult wild type, *sin-3(tm1276)* and *sin-3(syb2172)* mutant animals. Images are representative of a total of 6 animals imaged for wild type, 4 for *sin-3(syb2172)* and 5 for *sin-3(syb2172)*. Further examples for each genotype are displayed in Figure S1. Single mitochondria are indicated by arrows.

(B) Detailed view of enlarged mitochondria with aggregates. White arrows in A (panels a–j) indicate examples of individual mitochondria, black arrows in A (panels b, c, and e) and B indicate mitochondria with densely stained aggregates. Scale bars are indicated for each image.

(C) Quantification of perimeter, circularity and area of individual mitochondria from TEM images. For each worm, muscle mitochondria were analyzed on several TEM micrographs (at least 2–3 mitochondria on 25 to 60 images per condition), allowing the analysis of 72 mitochondria for wild type N2 ($n = 4$), 63 for *sin-3(tm1276)* ($n = 4$) and 180 for *sin-3(syb2172)* ($n = 4$). See also Figure S2.

is affected in these mutants (Figure 3E). Degradation of muscle proteins may also occur prematurely in these animals.[55] Because defects in muscle fibers are observed only in older *sin-3* mutant adults, while mitochondrial defects already appear at day 1, these results are consistent with a decline in mitochondrial network structure preceding muscle decline, as previously reported.[56,57]

Mitochondrial UPR is dampened in the absence of SIN-3

In response to mitochondrial stress, cells can trigger the mitochondrial unfolded protein response (UPR^{mt}) that transmits mitochondrial stress signals to the nucleus to regulate mitochondrial chaperone genes and other factors necessary for the recovery of damaged mitochondria.[58] Increased mitochondrial fragmentation in *sin-3* mutants suggests that SIN-3 may be required for mitochondrial homeostasis. We therefore asked whether UPR^{mt} is properly activated in *sin-3* mutant animals, using the *hsp-6* chaperone as a reporter (Haeussler and Conradt 2022).

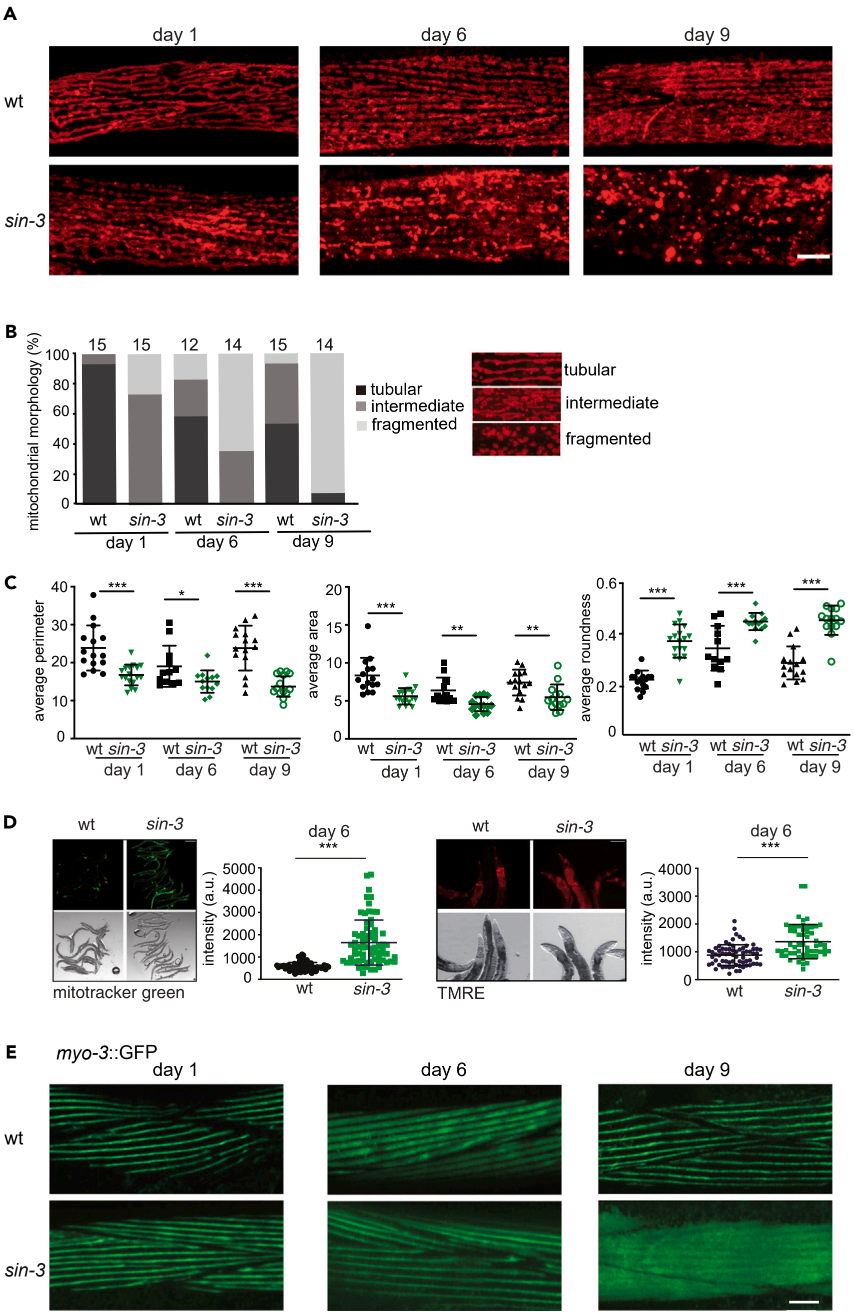

Figure 3. Altered mitochondria morphology and microfilament structure in *sin-3(tm1276)* muscle cells

(A) Representative confocal images of mitochondria morphology in body wall muscles expressing *myo-3p::tomm-20*Nter::wrmScarlet in wild type and *sin-3(tm1276)* mutant animals. Images were taken at day 1, 6 or 9 of adulthood. Scale bar: 10μm.

(B) Quantification of animals with the indicated muscle mitochondria phenotypes at day 1, 6, or 9 of adulthood. Total number of worms scored for each condition is indicated above bars.

(C) Quantification of morphological parameters of segmented mitochondria from wild type and *sin-3(tm1276)* at day 1, 6, or 9 of adulthood. Measured parameters are average perimeter, average area and average roundness (see STAR Methods for specifications). Between 12 and 15 animals were analyzed per condition. Data represents mean ± SD. Statistical differences were calculated using unpaired t test or Mann Whitney test (*$p < 0.05$, **$p < 0.007$, ***$p < 0.0001$).

(D) Quantification of Mitotracker Green and TMRE staining of wild type and *sin-3* (*tm1276*) mutants. Representative images of Mitotracker Green (left panel) and TMRE staining (right panel) are shown accompanied by the corresponding bright field images. Scale bar: 400 μm for Mitotracker Green and 100 μm for TMRE.

Figure 3. *Continued*

Data represent the mean ± SD of 2–3 independent replicates, where each data point represents one worm. Statistical differences were calculated using Mann Whitney test (***$p < 0.0001$).

(E) Representative confocal images of myofilament structure in body wall muscles expressing *myo-3*::GFP in wild type or *sin-3(tm1276)* mutant animals. Images were taken at day 1, 6, or 9 of adulthood. Scale bar: 10μm.

sin-3(tm1276) mutants carrying *hsp-6*::GFP were sterile, most likely due genetic interaction with a background mutation in the *hsp-6*::GFP bearing strain (Caehnorhabditis Genetics Center, GCG), so we used RNAi to deplete *sin-3. sin-3*(RNAi) alone had no reproducible effect on *hsp-6*::GFP expression (Figures 4A and 4B). Induction of mitochondrial stress by RNAi knockdown of the NADH ubiquinone oxidoreductase component *nuo-4*, or the mitochondrial ribosomal protein *mrps-5*, resulted in strong *hsp-6*::GFP expression in the intestine, as expected.[59] Simultaneous depletion of both *sin-3* and *nuo-4*, or *sin-3* and *mrps-5*, significantly decreased GFP expression in older animals at day 6 (Figure 4A), while no significant difference was observed at day 3 (Figure S3). RT-qPCR analysis confirmed knockdown of the respective genes in single and double RNAi experiments (Figure S3B). These results suggest that SIN-3 is required for a full response to mitochondrial stress depending of the animal's age. Interestingly, components of the NuRD chromatin remodeling complex have been shown to relocate to the nucleus upon mitochondrial stress[18] to influence the UPR^{mt}. Using a SIN-3:RFP translational fusion, we observed no obvious change in SIN-3 localization following mitochondrial stress (Figure S4).

Increased oxygen consumption in aged *sin-3* mutant animals

To understand how altered mitochondrial structure following loss of SIN-3 relates to mitochondrial function, we measured oxygen consumption in *sin-3(tm1276)* mutants. In *C. elegans*, oxygen consumption rates (OCRs) as a measure of ETC function can be accurately assessed using a Seahorse Analyzer with intact animals.[37,60] Wild type animals maintained a constant basal OCR from the young adult stage to day 6 of adulthood, although a tendency to reduce basal respiration during aging was apparent, as previously reported (Figure 5A, compare YA to D6).[61,62] By contrast, as *sin-3* mutants aged, basal OCR dramatically increased, so that at day six of adulthood it was more than 2-fold higher in *sin-3* mutants compared to wild type (Figure 5A, D6).

We next measured maximal respiratory capacity following mitochondrial uncoupling by the addition of carbonyl cyanide-*p*-trifluoromethoxyphenylhydrazone (FCCP). In *sin-3* young adults, maximal OCR was similar to wild type, but we again observed a significant increase in aged *sin-3* mutants compared to age-matched wild type (Figure 5B). Moreover, in old *sin-3* mutants the observed increase in basal respiration was proportionally larger than the increase in maximal respiratory capacity (Figures 5A and 5B). Consequently mitochondrial spare capacity, which characterizes the ability of mitochondria to meet extra energy requirements beyond the basal level,[63] was reduced compared to old wild type worms (Figure 5C). Increased OCR could be a side effect of partial mitochondrial uncoupling.[64] We note, however, that *ucp-4*, the single mitochondrial uncoupling protein in *C. elegans*, was not present in the list of *sin-3* misregulated genes, while expression of the *ant-1.1* ADP/ATP translocator whose activity can also result in mitochondrial uncoupling was down (Table S1).[65,66] Consistent with depletion of SIN-3 affecting mitochondrial integrity, in extracts from *sin-3(tm1276)* animals we observed a trend toward decreased levels of conserved electron transport proteins, detected using antibodies against the highly conserved mammalian complex III subunit UQCRC2 and complex II subunit SDHB1. Protein abundance of the ATP synthase ATP5 was less affected (Figures 5D and 5E).

sin-3 inactivation does not alter levels of TCA cycle metabolites, but results in a signature of mitochondrial stress

The previous results clearly establish that *sin-3* knockdown or deletion leads to defective mitochondrial function. Because mitochondria are a hub for biosynthetic processes, we used metabolomic analysis to probe for SIN-3-dependent metabolic changes in animals carrying the *sin-3(tm1276)* loss of function allele. We used young adult animals, the same stage used for transcriptomics analysis and TEM observations. We chose this allele because the sterility of *sin-3(syb2172)* null mutants precluded growing the large number of animals required for this type of analysis. We observed no significant change in the abundance of TCA cycle intermediates detected, including succinyl-CoA, alpha-keto-glutaric acid, succinic acid, fumaric acid, and malic acid (Table S4; Figures S5A and S5B). Although two peaks putatively annotated as glycolytic intermediates glucose-6-P and glucose-1-P showed a significant reduction in *sin-3* mutants, the downstream metabolite fructose-1,6-bis-P showed no difference (Table S4; Figure S5B). Glucose-1-P is a metabolite of gluconeogenesis and starch and sucrose metabolism. *C. elegans* can store excess energy in the form of trehalose and glycogen.[67] However, we detected no significant change in UDP-glucose (an intermediary for glycogen and trehalose synthesis), trehalose-6-P, or trehalose in *sin-3* mutant animals (Table S4; Figure S5B). Together, these results suggest that in young animals the absence of SIN-3 has little or no influence on energy metabolism. This was further corroborated by only minor changes in lipid metabolism intermediates including short-chain acyl-CoA and short-chain acyl-carnitine species (Table S5; Figure S5A). Nonetheless, it is important to note that metabolite levels are only indicative of changes in metabolic flux, defined as the turnover rate of metabolites through enzymatically controlled pathways.[68] Increased mitochondrial fragmentation may lead to changes or redirection of metabolic fluxes without altering metabolite levels.

In contrast to the previous results, significant changes in amino acid metabolism were detected: aspartic acid levels significantly decreased in *sin-3* mutants, while proline, threonine, lysine, serine, and citrulline increased (Figures 6A and S5C; Table S5). Interestingly, decreased aspartic acid and increased serine have been shown to be a signature of mitochondrial stress.[69] No changes in glutathione (GSH) and glutathione disulfide (GSSG), both associated with oxidative stress, were detected (Table S5; Figure S5C). An increase in sarcosine and dimethylarginine was also detected (Table S5; Figure S5C).

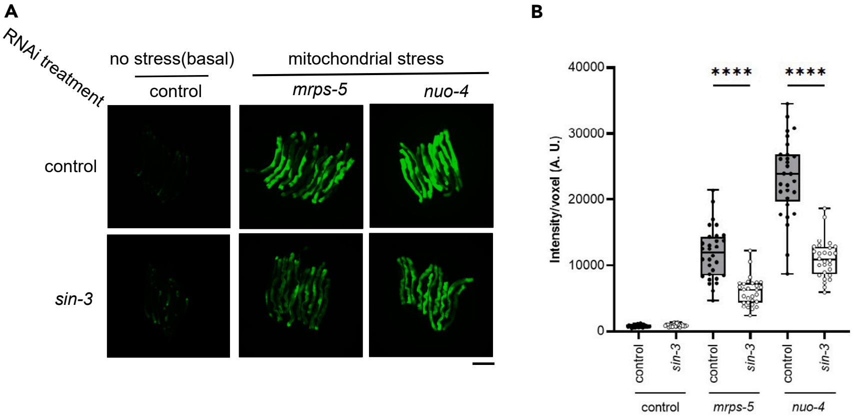

Figure 4. Loss of *sin-3* dampens the response to mitochondrial stress

(A) Images of wild type or *sin-3*(RNAi) animals expressing *hsp-6p*::GFP reporter under basal conditions (no stress), or following mitochondrial stress induced by RNAi knock-down of mitochondrial genes *mrps-5* and *nuo-4*. Parent worms were grown on HT115 control or *sin-3* RNAi from hatch until the adult stage. F1 offspring were then grown from hatch on control, *nuo-4* or *mrps-5* single RNAi, or *sin-3*, *sin-3* + *nuo-4*, and *sin-3* + *mrps-5* double RNAi. GFP expression was measured 5 days after eggs were laid. Scale bar: 300μm.

(B) Quantification of *hsp-6p*::GFP expression. Data are representative of one of two independent experiments with 30 animals per condition each. Boxplots with median corresponding to the middle of the box, first and third quartiles to the edges of the box, and lines extreme values. Significance was calculated using Mann-Whitney test, *p* value * <0.05, **** <0.0001. See also Figure S3.

SIN-3 is required to maintain polyamine homeostasis

Both serine and sarcosine are connected to one-carbon metabolism, which encompasses both the folate and methionine cycles to generate one-carbon units (methyl groups) that are used for the biosynthesis of important precursors and for methylation reactions.[70] While no changes in folate cycle intermediates folate, 5-methyl tetrahydrofolic (mTHF) or dihydrofolic (DHF) acid were found (Table S5; Figure S5D), a significant decrease in the methionine cycle metabolite S-adenosylmethionine (SAM) was observed (Figures 6B and S5D; Table S5).

SAM is the major methyl donor in the cell and is critical for the synthesis of phosphatidylcholine, an important component of cellular membranes,[71] as well as for the methylation of DNA, RNA, and histones through transmethylation.[70] SAM is also connected to polyamine synthesis through the activity of *S*-adenosylmethionine decarboxylase (adoMETDC/*smd-1*) that results in the production of decarboxylated *S*-adenosylmethioninamine (dc-SAM) (Figure 6C). Spermidine synthase (SPDS/*spds-1*), a key enzyme in the pathway, then catalyzes the transfer of an aminopropyl moiety of dcSAM to putrescine, resulting in the formation of spermidine and 5′-methylthioadenosine (MTA). Putrescine is provided by another key enzyme, ornithine decarboxylase (ODC/*odc-1*) (Figure 6C). Interestingly while the abundance of downstream metabolites of the transmethylation pathway, S-adenosyl homocysteine (SAH) and cystathionine, was not altered in *sin-3* mutants (Figures 6B and S5E; Table S5), both dcSAM and MTA were strongly reduced (Table S5; Figure S5E). Levels of neither arginine nor ornithine, two precursors of putrescine, nor putrescine itself was altered in *sin-3* mutants (Figures 6B and S5C; Table S5), while we detected a large increase in both spermidine and N-Acetyl-spermine, the degradation products of spermine and spermidine, respectively (Figures 6C and S5E; Table S5). Spermine could not be detected in our analysis. Together, these results suggest that in the absence of SIN-3, the metabolic flux is shifted from transmethylation to polyamine biosynthesis. Consistent with a shift in metabolic flux toward the synthesis of polyamines, the abundance of N-acetylputrescine, a degradation product of putrescine, was unaltered in our analyses (Table S5; Figure S5D). The abundance of another polyamine, cadaverine, was also increased in *sin-3* mutants (Figures 6D and S5E; Table S5). Cadaverine is produced by the decarboxylation of lysine, and is also more abundant in *sin-3* mutants (Figures 6D and S5C; Table S5). No dedicated lysine decarboxylase has been annotated in *C. elegans* to date, but *odc-1* could potentially fulfill this function.[72]

Another lysine catabolite whose abundance increased in *sin-3* mutants is saccharopine, while aminoadipic acid (L-2-Aminoadipate), the metabolite further downstream, showed a slight but not significant increase (Figures 6D and S5C; Table S5). Because lysine degradation via the formation of saccharopine is confined to the mitochondria,[73] a potential blockage in its degradation due to defective mitochondria could increase its abundance (Figure 6D).

Transcriptomics analysis reveals deregulation of metabolic pathways

The previous metabolic analysis was conducted on *sin-3(tm1276)* mutant animals at the young adult stage. Close inspection of the previously published list of genes misregulated in these mutants animals at the same stage[36] identified candidates whose misexpression correlates with the observed metabolic changes (Figure 6C). The ornithine decarboxylase *odc-1*, which converts ornithine to putrescine,[74] was strongly upregulated in *sin-3(tm1276)* mutants (log2FC 1.15, $p = 4.09e\text{-}06$), as was the spermidine synthase *spds-1* (log2FC 2.29, $p = 2.88e\text{-}19$). Regulation of polyamine synthesis is mainly achieved by controlling the activity of ornithine decarboxylase through its inhibitor antizyme, the binding of which disrupts ODC enzymatic activity and targets it for ubiquitin-independent degradation.[75] Significantly, the *C. elegans* homologue of antizyme, *oaz-1*, was significantly downregulated (log2FC −0.86, $p = 4.29e\text{-}32$), potentially leading to increased ODC-1 activity and

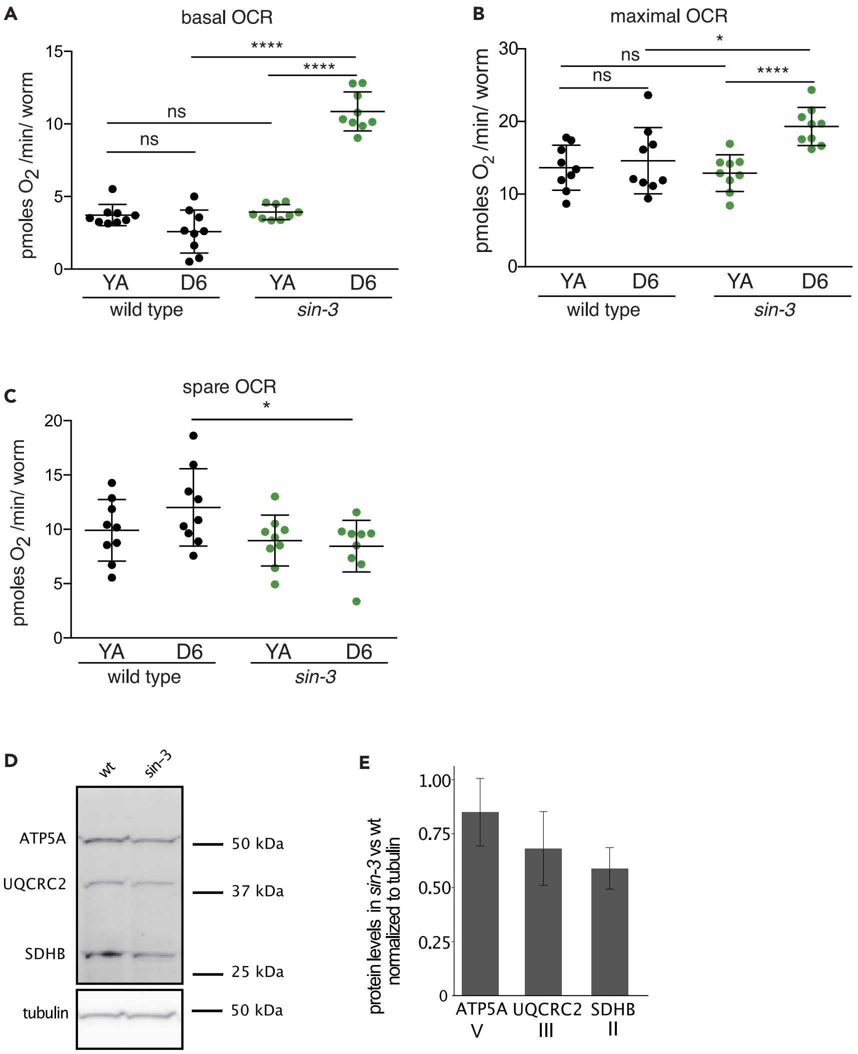

Figure 5. Oxygen consumption rate (OCR) and abundance of mitochondrial respiratory chain subunits in *sin-3(tm1276)* mutants

(A) Basal OCR of wild type and *sin-3* mutants at the young adult (YA) stage and at day 6 of adulthood (D6).

(B) Maximal OCR of wild type and *sin-3* mutants at the YA stage and at D6 of adulthood.

(C) Spare respiratory capacity of wild type and *sin-3* mutants at the YA stage and at D6 of adulthood. Significance was calculated using unpaired *t*-test or, when appropriate, Mann-Whitney test, *p* value * <0.05, **** <0.0001.

(D) Western blot showing SDHB-1/SDHB (complex II), CTC-1/UQCRC2 (complex IV), and ATP-2/ATP5A (complex V) protein levels in total protein extracts from wild type and *sin-3(tm1276)* L4-young adult worms detected by fluorescence.

(E) Levels of each protein were quantified with ImageJ and normalized to tubulin levels. Bar plot represents the mean of two to three independent biological replicates; error bars correspond to SD.

spermidine biosynthesis in these mutants. Because *odc-1* may also decarboxylate lysine to produce cadaverin,[72] its increased activity could contribute to the observed increase in cadaverin levels. The polyamine oxidase (PAO) *hpo-15* is instead upregulated in *sin-3(tm1276)* mutants (log2FC 1.74, *p* = 6.56e-08). N-acetylspermine and N-acetylspermidine, metabolites of spermine and spermidine, respectively, are used as substrates by PAO to produce H_2O_2 and either spermidine or putrescine, depending on the starting substrate. An increased *hpo-15* expression may therefore also contribute to both the increase in spermidine levels and increased sensitivity to oxidative stress in *sin-3* mutant animals, as observed in mammalian cells.[76] Interestingly, spermidine serves as the sole biosynthetic precursor for hypusination, a post-translational modification that is an integral component of eukaryotic translation initiation factor 5A (eIF5A).[77] Genes encoding the two enzymes required for hypusination, the deoxyhypusine synthase *dhps-1* and the deoxyhypusine hydroxylase *dohh-1*, were both upregulated in *sin-3(tm1276)* mutants (log2FC 0.7390, *p* = 7.89e-27 and 0.44, *p* = 2.60e-18, respectively). Of these genes only *oaz-1* and *hpo-15* are included in the list of genes commonly misregulated in the two *sin-3* alleles (Table 1), most likely reflecting experimental differences between the two transcriptomics analyses.[34] Altogether our data are consistent with deregulation of specific metabolic genes in *sin-3(tm1276)* mutants

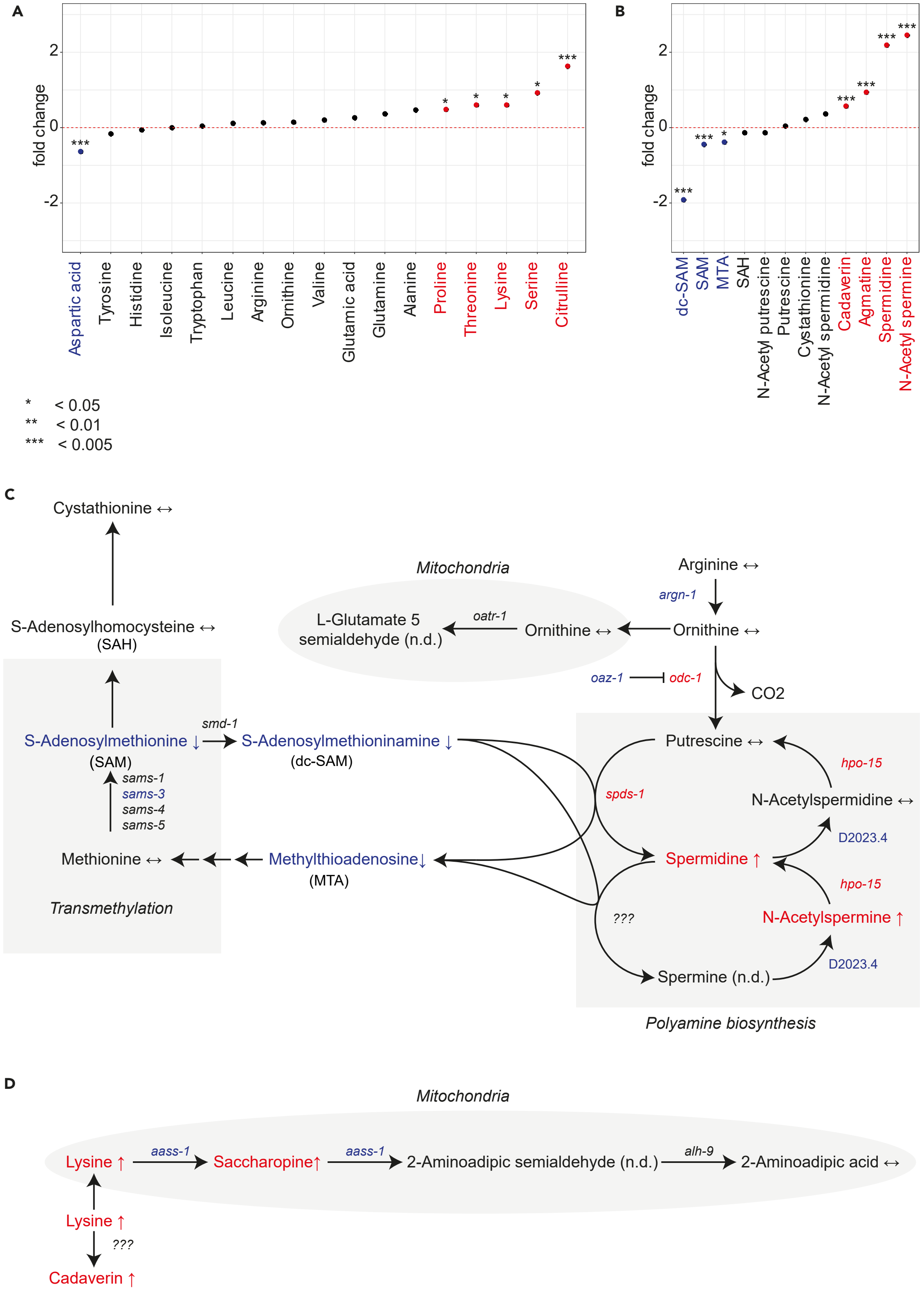

Figure 6. Metabolic alterations in *sin-3(tm1276)* mutant young adult animals and their related pathways

Changes in amino acid metabolites (A) and polyamine-related metabolites (B) in *sin-3(tm1276)* mutants at the young adult stage. Welch test, *p*-value * <0.05, ** <0.01, *** <0.005.

Figure 6. *Continued*

(C) Schematic representation of biosynthetic pathway for arginine-derived polyamines.

(D) Biosynthetic pathway of cadaverine and lysine degradation. Arrows and colors in (C) and (D) indicate significant changes for metabolites and metabolic genes (blue = down, red = up). Areas shaded in gray indicate specific pathways, or reactions that take place in the mitochondria. See also Figure S5 and Tables S1, S2, S3, S4, and S5.

contributing to the observed changes in polyamine flux. Whether these changes are a cause or consequence of the observed changes in mitochondrial dynamics and respiration remains to be established.

DISCUSSION

The SIN3 corepressor has been linked to mitochondrial function in several models, but how its loss alters mitochondrial dynamics and metabolism in the context of an entire organism has not been explored. Here, using two different *sin-3* mutant alleles, we show that in *C. elegans* adult animals partial or complete loss of *sin-3* function results in increased expression of genes encoded by the mitochondrial genome and an overall decrease in the expression of nuclear-encoded mitochondrial genes, potentially leading to nuclear-mitochondrial imbalance. We show that the altered expression of mitochondrial genes is associated with increased mitochondrial fragmentation in all tissues examined, increased oxygen consumption, and metabolic changes, including a pronounced shift in metabolic flux from methionine to polyamine biosynthesis. Together our data identify SIN-3 as a key regulator of mitochondrial dynamics and polyamine homeostasis.

Knockdown of SIN3 in different systems results in strikingly similar phenotypes. Lower ATP levels were observed following reduction of SIN3 activity in yeast in all media conditions, in *Drosophila* cultured cells in nutrient-depleted conditions, and in *C. elegans* adults.[20,33] Both *Drosophila* and *C. elegans* adult animals show an increase in oxidative stress.[22,78] Deregulation of mitochondrial genes was reported following either knockdown or overexpression of SIN3 in cultured *Drosophila* cells,[20,21] or conditional *mSin3A* knock-out in primary cell culture.[79] Our transcriptomics analysis on *sin-3(tm1276)* and *sin-3(syb2178)* mutant animals revealed that expression of respiratory complex I subunits encoded by the mitochondrial genome is strongly increased in both mutants, while expression of nuclear-encoded subunits of additional complexes is downregulated. The expression of additional genes with important roles in mitochondrial function, including mitochondrial ribosomal proteins and the *tomm-1* translocase is also significantly decreased in *sin-3* mutants. Importantly, SIN-3 binding on a number of downregulated genes suggests that SIN-3 may positively regulate their expression, as observed for SIN3 in other contexts.[34,80–82]

The nucleus and mitochondria constantly communicate to adjust their activities in order to ensure cellular homeostasis,[83] and reducing the expression of a single major ribosomal nuclear protein (MRP) is sufficient to induce a stoichiometric imbalance between nuclear and mitochondrial-DNA encoded ETC subunits[59] and activate the UPR^{mt}.[84] Interestingly, the *C. elegans* histone deacetylase *hda-1*, encoding a conserved component of SIN3 complexes,[34,36] was shown to be required for this stress response.[85] We observed that expression of the UPR^{mt} reporter *hsp-6* was dampened following induction of mitochondrial stress in *sin-3* knockdown animals, but only in old adults. Therefore, it is likely that HDA-1 acts in a context other than SIN-3 in the UPR^{mt}, most likely the NuRD histone deacetylase complex.[18]

One of the most striking phenotypes we observed is that either reduced SIN-3 function or its complete absence results in a dramatic increase in mitochondrial fragmentation, observed by TEM in all tissues examined, including muscle, intestine, pharynx, hypodermis, and germ cells, and through live imaging in muscle cells. The ability to transition between fission/fusion states is essential for mitochondrial function in cellular bioenergetics, regulation of intracellular Ca^{2+}, and cellular stress responses.[86] Fusion allows damaged mitochondria to mitigate stress by mixing contents, while fission contributes to quality control of damaged mitochondria by budding off deteriorating components for targeted breakdown via autophagy or mitophagy. The increased fragmentation we observe is consistent with a defect in the maintenance of mitochondrial homeostasis. We also observed examples of enlarged mitochondria, another hallmark of mitochondrial damage,[87] and the accumulation of electron-dense material in mitochondria that may represent iron deposits or misfolded proteins. Similar aggregates were observed by TEM in *C. elegans* following acute heat stress,[42] in sperm-derived mitochondria before their elimination by mitophagy,[43,44] and in the mitochondria of worms containing mutations in *eat-3*/OPA1 and *fzo-1*/mfn1 fusion genes,[88] supporting a link between their formation and mitochondrial morphological defects. Alternatively, these aggregates may represent iron deposits such as those observed in the mitochondria of a mouse model of Friedrich ataxia[39,89] and congenital sideroblastic anemia.[90] Interestingly mitochondrial iron overload promotes ROS production, as observed in *sin-3* mutants (Pandey et al., 2018), and is associated with mitochondrial dysfunction and oxidative damage.[91] Regardless of the underlying cause, disruption of mitochondria homeostasis, as observed in *sin-3* mutant animals, is likely to have major consequences for mitochondrial health and function.

The rate of oxygen consumption is another measure of mitochondrial activity, and we observed significant differences in respiration in *sin-3(tm1276)* mutants. While neither basal nor maximal OCRs were affected in mutant young adults, both were significantly elevated in older mutants compared to wild type. Conversely, mitochondrial spare respiratory capacity was reduced in these mutants. Spare respiratory capacity can be viewed as a determinant of mitochondrial fitness and correlates with level of mitochondrial plasticity, allowing bioenergetic adaptability in response to pathophysiological stress conditions.[63] Its decrease in older *sin-3(tm1276)* mutants is consistent with mitochondrial dysfunction in these animals.

Increased basal and maximal oxygen consumption in old *sin-3(tm1276)* animals contrasts with wild type, in which oxygen consumption has a tendency to decrease with age.[60,62] Interestingly, a similar increase during aging was observed in worms lacking the mitochondrial prohibitin (PHB) complex subunits *phb-1* and *phb-2*.[92] Like *sin-3* mutants, prohibiting mutants are also short-lived and show severely fragmented mitochondria.[93,94] PHB plays a prominent role in the response to mitochondrial stress, quality control, biogenesis, and degradation,[95] and its expression is induced by metabolic stress resulting from mito-nuclear imbalance, but not other cellular stresses.[96] It was suggested that PHB may act as chaperone in respiratory complex assembly,[97] with its loss affecting complex integrity. Likewise, imbalance between nuclear- and mitochondrial-encoded subunits in *sin-3* mutants could result in defects in respiratory complex assembly. In this context, increased oxygen consumption may reflect compensatory activity from properly assembled supercomplexes, or mitochondrial adaptation resulting in an increase in mitochondrial mass,[98] as we observe in *sin-3* mutants.

Consistent with mitochondrial fragmentation being generally associated with metabolic dysfunction and disease,[86] metabolomic analysis revealed dramatic changes in the levels of several metabolites in *sin-3(tm1276)* mutants. One of the most striking differences we observed is an increase in the polyamines spermine and cadaverine. Polyamine biosynthesis is tightly controlled, and changes in polyamine levels can have dramatic consequences on physiology, with established links between polyamine metabolism and human diseases including cancer and diabetes.[99] Spermine is a potent free radical scavenger and an important antioxidant,[100,101] and in *C. elegans*, spermidine has been shown to inhibit neurodegeneration and have pro-longevity effects.[102] However, spermidine or spermine in excess can also have deleterious consequences on animal physiology,[101,103–105] and SIN-3 inactivation or knock-down in *C. elegans* is associated with sterility, decreased longevity, and increased oxidative stress (Sharma et al., 2018). Our expression profiling suggests that decreased expression of the *oaz-1* antizyme, a critical regulator of polyamine biosynthesis,[75] may be a major contributor to the effect of SIN3 knockdown on polyamine homeostasis.

Among a broad range of functions, spermidine serves as the sole biosynthetic precursor for hypusination, a post-translational modification that is an integral component of eukaryotic translation initiation factor 5A (eIF5A).[106] Polyamine levels are elevated in most cancers, and hypusinated eIF5A is a critical regulator of cell growth.[104] More recently, hypusinated eIF5A was shown to promote expression of mitochondrial proteins in macrophages,[107] suggesting that it may also alter mitochondrial activity in both normal and cancer cells. This raises the intriguing possibility that increased spermidine biosynthesis and eIF5A hypusylation in *sin-3* mutants may be part of a mechanism to increase the expression of mitochondrial proteins in response to mitochondrial damage.

Further evidence for a shift in metabolic flux toward polyamine biosynthesis comes from the analysis of downstream metabolites in the transmethylation pathway. Conversion of SAM to dcSAM provides necessary amino-propyl groups to sustain polyamine synthesis.[104] The methionine salvage pathway (MSP) recycles one carbon unit lost during polyamine synthesis back to the methionine cycle for SAM replenishment. In addition to showing a strong decrease in dcSAM, and a smaller but significant decrease in SAM, *sin-3* mutants also show reduced activity of the salvage pathway, as illustrated by a decrease in levels of the MSP intermediate methyladenosine (Figure 6C). Interestingly, in Prostate cancer (PCa) cells, which have an intrinsically high polyamine metabolic flux and therefore rely heavily on the methionine salvage pathway, MSP inhibition while maintaining high polyamine flux was shown to be an effective cancer therapy by blocking the ability of the cell to mitigate this stress, leading to cell death.[108] In other tumor cell types, by contrast, defects in the MSP were found to increase polyamine levels, highlighting how the stress that is generated by metabolic perturbations is often context-dependent.[104] Because increasing evidence points to a causal link between mitochondrial dysfunction and pediatric neurodevelopmental disorders, our study may also suggest new lines of investigation into the interconnected links between SIN3, mitochondrial homeostasis, and metabolism in the context of SIN3-related disorders.

Limitations of the study

While changes in respiration were only observed in older *sin-3* mutant animal, the transcriptomics and metabolomic studies reported here were carried out on young adults, so that relevant changes that may occur later in life could have been missed. We also do not know whether the metabolic changes reported for *sin-3* mutants are a cause or consequence of mitochondrial defects. Metabolomic analysis of older animals, as well as genetic analysis, will help clarify these outstanding questions.

STAR★METHODS

Detailed methods are provided in the online version of this paper and include the following:

- KEY RESOURCES TABLE
- RESOURCE AVAILABILITY
    - Lead contact
    - Materials availability
    - Data and code availability
- EXPERIMENTAL MODEL AND STUDY PARTICIPANT DETAILS
- METHOD DETAILS
    - Gene enrichment analysis
    - Transmission electron microscopy
    - Quantification of muscle mitochondria and imaging of myofilament structure
    - TMRE and Mitotracker staining
    - Activation of UPRmt by RNAi treatment
    - Oxygen consumption measurements
    - Western blot analysis

  - ○ Metabolite extraction and profiling
  - ○ Metabolite data analysis
- ● QUANTIFICATION AND STATISTICAL ANALYSIS

SUPPLEMENTAL INFORMATION

Supplemental information can be found online at https://doi.org/10.1016/j.isci.2024.109789.

ACKNOWLEDGMENTS

F.P. was supported by ANR (Agence Nationale de la Recherche) grant N° 19-CE12-0025-01 and the Centre National de la Recherche Scientifique. M.A.S. was funded through grants from the Ministerio de Ciencia, Innovación y Universidades, the Agencia Estatal de Investigación (AEI) PID 2019-104145GB-I00. G.M. laboratory receives institutional funding from the Centre National de la Recherche Scientifique and the Université de Rennes. TEM imaging was performed at the Microscopy Rennes imaging Center (Biosit, Rennes, France), a member of the national infrastructure France-BioImaging supported by the French National Research Agency (ANR-10-INBS-04). Thanks to Emiliano Ricci for OXPHOS antibodies, Florence Solari for strains. Special thanks to Liesbeth de Jong for the graphical abstract.

AUTHOR CONTRIBUTIONS

P.F., F.P., and M.A.S. conceived and designed experiments, P.F., M.G., M.J.R.P., M.A.S., and C.B. performed experiments and analyzed the data, G.M. conceived and supervised E.M. experiments and quantification with O.N. and M.W. conceived, performed, and analyzed metabolomic studies, F.P. wrote the paper, M.A.S., M.W., and G.M. contributed to specific sections, and all authors contributed to figures. F.P. and M.A.S. share responsibility for all aspects of this work.

DECLARATION OF INTERESTS

The authors declare no competing interests.

Received: August 14, 2023
Revised: January 30, 2024
Accepted: April 16, 2024
Published: April 22, 2024

REFERENCES

1. Signes, A., and Fernandez-Vizarra, E. (2018). Assembly of mammalian oxidative phosphorylation complexes I–V and supercomplexes. Essays Biochem. *62*, 255–270. https://doi.org/10.1042/EBC20170098.
2. Richter-Dennerlein, R., Oeljeklaus, S., Lorenzi, I., Ronsör, C., Bareth, B., Schendzielorz, A.B., Wang, C., Warscheid, B., Rehling, P., and Dennerlein, S. (2016). Mitochondrial Protein Synthesis Adapts to Influx of Nuclear-Encoded Protein. Cell *167*, 471–483.e10. https://doi.org/10.1016/j.cell.2016.09.003.
3. DiMauro, S., and Schon, E.A. (2003). Mitochondrial Respiratory-Chain Diseases. N. Engl. J. Med. *348*, 2656–2668. https://doi.org/10.1056/NEJMra022567.
4. Fernandez-Vizarra, E., and Zeviani, M. (2021). Mitochondrial disorders of the OXPHOS system. FEBS Lett. *595*, 1062–1106. https://doi.org/10.1002/1873-3468.13995.
5. Reeve, A.K., Krishnan, K.J., and Turnbull, D. (2008). Mitochondrial DNA Mutations in Disease, Aging, and Neurodegeneration. Ann. N. Y. Acad. Sci. *1147*, 21–29. https://doi.org/10.1196/annals.1427.016.
6. Taanman, J.-W. (1999). The mitochondrial genome: structure, transcription, translation and replication. Biochim. Biophys. Acta *1410*, 103–123. https://doi.org/10.1016/S0005-2728(98)00161-3.
7. Ali, A.T., Boehme, L., Carbajosa, G., Seitan, V.C., Small, K.S., and Hodgkinson, A. (2019). Nuclear genetic regulation of the human mitochondrial transcriptome. Elife *8*, e41927. https://doi.org/10.7554/eLife.41927.
8. Barshad, G., Blumberg, A., Cohen, T., and Mishmar, D. (2018). Human primitive brain displays negative mitochondrial-nuclear expression correlation of respiratory genes. Genome Res. *28*, 952–967. https://doi.org/10.1101/gr.226324.117.
9. Mercer, T.R., Neph, S., Dinger, M.E., Crawford, J., Smith, M.A., Shearwood, A.-M.J., Haugen, E., Bracken, C.P., Rackham, O., Stamatoyannopoulos, J.A., et al. (2011). The human mitochondrial transcriptome. Cell *146*, 645–658. https://doi.org/10.1016/j.cell.2011.06.051.
10. Quirós, P.M., Mottis, A., and Auwerx, J. (2016). Mitonuclear communication in homeostasis and stress. Nat. Rev. Mol. Cell Biol. *17*, 213–226. https://doi.org/10.1038/nrm.2016.23.
11. Anderson, N.S., and Haynes, C.M. (2020). Folding the Mitochondrial UPR into the Integrated Stress Response. Trends Cell Biol. *30*, 428–439. https://doi.org/10.1016/j.tcb.2020.03.001.
12. Matilainen, O., Quirós, P.M., and Auwerx, J. (2017). Mitochondria and Epigenetics - Crosstalk in Homeostasis and Stress. Trends Cell Biol. *27*, 453–463. https://doi.org/10.1016/j.tcb.2017.02.004.
13. Yang, R., Li, Y., Wang, Y., Zhang, J., Fan, Q., Tan, J., Li, W., Zou, X., and Liang, B. (2022). NHR-80 senses the mitochondrial UPR to rewire citrate metabolism for lipid accumulation in Caenorhabditis elegans. Cell Rep. *38*, 110206. https://doi.org/10.1016/j.celrep.2021.110206.
14. Rolland, S., and Conradt, B. (2022). Genetic screen identifies non-mitochondrial proteins involved in the maintenance of mitochondrial homeostasis. MicroPubl. Biol. *2022*. https://doi.org/10.17912/micropub.biology.000562.
15. Rolland, S.G., Schneid, S., Schwarz, M., Rackles, E., Fischer, C., Haeussler, S., Regmi, S.G., Yeroslaviz, A., Habermann, B., Mokranjac, D., et al. (2019). Compromised Mitochondrial Protein Import Acts as a Signal for UPRmt. Cell Rep. *28*, 1659–1669.e5. https://doi.org/10.1016/j.celrep.2019.07.049.
16. Lionaki, E., Gkikas, I., Daskalaki, I., Ioannidi, M.-K., Klapa, M.I., and Tavernarakis, N. (2022). Mitochondrial protein import determines lifespan through metabolic reprogramming and *de novo* serine biosynthesis. Nat. Commun. *13*, 651. https://doi.org/10.1038/s41467-022-28272-1.
17. Tian, Y., Garcia, G., Bian, Q., Steffen, K.K., Joe, L., Wolff, S., Meyer, B.J., and Dillin, A. (2016). Mitochondrial Stress Induces Chromatin Reorganization to Promote

Longevity and UPR mt. Cell *165*, 1197–1208. https://doi.org/10.1016/j.cell.2016.04.011.

18. Zhu, D., Wu, X., Zhou, J., Li, X., Huang, X., Li, J., Wu, J., Bian, Q., Wang, Y., and Tian, Y. (2020). NuRD mediates mitochondrial stress-induced longevity via chromatin remodeling in response to acetyl-CoA level. Sci. Adv. *6*, eabb2529. https://doi.org/10.1126/sciadv.abb2529.
19. Chaubal, A., and Pile, L.A. (2018). Same agent, different messages: insight into transcriptional regulation by SIN3 isoforms. Epigenet. Chromatin *11*, 17. https://doi.org/10.1186/s13072-018-0188-y.
20. Barnes, V.L., Strunk, B.S., Lee, I., Hüttemann, M., and Pile, L.A. (2010). Loss of the SIN3 transcriptional corepressor results in aberrant mitochondrial function. BMC Biochem. *11*, 26. https://doi.org/10.1186/1471-2091-11-26.
21. Pile, L.A., Spellman, P.T., Katzenberger, R.J., and Wassarman, D.A. (2003). The SIN3 Deacetylase Complex Represses Genes Encoding Mitochondrial Proteins. J. Biol. Chem. *278*, 37840–37848. https://doi.org/10.1074/jbc.M305996200.
22. Sharma, M., Pandey, R., and Saluja, D. (2018). ROS is the major player in regulating altered autophagy and lifespan in sin-3 mutants of C. elegans. Autophagy *14*, 1239–1255. https://doi.org/10.1080/15548627.2018.1474312.
23. Scoville, D.W., Cyphert, H.A., Liao, L., Xu, J., Reynolds, A., Guo, S., and Stein, R. (2015). MLL3 and MLL4 Methyltransferases Bind to the MAFA and MAFB Transcription Factors to Regulate Islet β-Cell Function. Diabetes *64*, 3772–3783. https://doi.org/10.2337/db15-0281.
24. Yang, X., Graff, S.M., Heiser, C.N., Ho, K.-H., Chen, B., Simmons, A.J., Southard-Smith, A.N., David, G., Jacobson, D.A., Kaverina, I., et al. (2020). Coregulator Sin3a Promotes Postnatal Murine β-Cell Fitness by Regulating Genes in Ca2+ Homeostasis, Cell Survival, Vesicle Biosynthesis, Glucose Metabolism, and Stress Response. Diabetes *69*, 1219–1231. https://doi.org/10.2337/db19-0721.
25. To, T.-L., Cuadros, A.M., Shah, H., Hung, W.H.W., Li, Y., Kim, S.H., Rubin, D.H.F., Boe, R.H., Rath, S., Eaton, J.K., et al. (2019). A Compendium of Genetic Modifiers of Mitochondrial Dysfunction Reveals Intra-organelle Buffering. Cell *179*, 1222–1238.e17. https://doi.org/10.1016/j.cell.2019.10.032.
26. Balasubramanian, M., Dingemans, A.J.M., Albaba, S., Richardson, R., Yates, T.M., Cox, H., Douzgou, S., Armstrong, R., Sansbury, F.H., Burke, K.B., et al. (2021). Comprehensive study of 28 individuals with SIN3A-related disorder underscoring the associated mild cognitive and distinctive facial phenotype. Eur. J. Hum. Genet. *29*, 625–636. https://doi.org/10.1038/s41431-020-00769-7.
27. Latypova, X., Vincent, M., Mollé, A., Adebambo, O.A., Fourgeux, C., Khan, T.N., Caro, A., Rosello, M., Orellana, C., Niyazov, D., et al. (2021). Haploinsufficiency of the Sin3/HDAC corepressor complex member SIN3B causes a syndromic intellectual disability/autism spectrum disorder. Am. J. Hum. Genet. *108*, 929–941. https://doi.org/10.1016/j.ajhg.2021.03.017.
28. Witteveen, J.S., Willemsen, M.H., Dombroski, T.C.D., van Bakel, N.H.M., Nillesen, W.M., van Hulten, J.A., Jansen, E.J.R., Verkaik, D., Veenstra-Knol, H.E., van Ravenswaaij-Arts, C.M.A., et al. (2016). Haploinsufficiency of MeCP2-interacting transcriptional co-repressor SIN3A causes mild intellectual disability by affecting the development of cortical integrity. Nat. Genet. *48*, 877–887. https://doi.org/10.1038/ng.3619.
29. Bansal, N., Petrie, K., Christova, R., Chung, C.-Y., Leibovitch, B.A., Howell, L., Gil, V., Sbirkov, Y., Lee, E., Wexler, J., et al. (2015). Targeting the SIN3A-PF1 interaction inhibits epithelial to mesenchymal transition and maintenance of a stem cell phenotype in triple negative breast cancer. Oncotarget *6*, 34087–34105. https://doi.org/10.18632/oncotarget.6048.
30. Bansal, N., David, G., Farias, E., and Waxman, S. (2016). Emerging Roles of Epigenetic Regulator Sin3 in Cancer. Adv. Cancer Res. *130*, 113–135. https://doi.org/10.1016/bs.acr.2016.01.006.
31. Farias, E.F., Petrie, K., Leibovitch, B., Murtagh, J., Chornet, M.B., Schenk, T., Zelent, A., and Waxman, S. (2010). Interference with Sin3 function induces epigenetic reprogramming and differentiation in breast cancer cells. Proc. Natl. Acad. Sci. USA *107*, 11811–11816. https://doi.org/10.1073/pnas.1006737107.
32. Lewis, M.J., Liu, J., Libby, E.F., Lee, M., Crawford, N.P.S., and Hurst, D.R. (2016). SIN3A and SIN3B differentially regulate breast cancer metastasis. Oncotarget *7*, 78713–78725. https://doi.org/10.18632/oncotarget.12805.
33. Pandey, R., Sharma, M., and Saluja, D. (2018). SIN-3 as a key determinant of lifespan and its sex dependent differential role on healthspan in Caenorhabditis elegans. Aging *10*, 3910–3937. https://doi.org/10.18632/aging.101682.
34. Robert, V.J., Caron, M., Gely, L., Adrait, A., Pakulska, V., Couté, Y., Chevalier, M., Riedel, C.G., Bedet, C., and Palladino, F. (2023). SIN3 acts in distinct complexes to regulate the germline transcriptional program in C. elegans. Development *150*, dev201755. https://doi.org/10.1242/dev.201755.
35. Holdorf, A.D., Higgins, D.P., Hart, A.C., Boag, P.R., Pazour, G.J., Walhout, A.J.M., and Walker, A.K. (2020). WormCat: An Online Tool for Annotation and Visualization of *Caenorhabditis elegans* Genome-Scale Data. Genetics *214*, 279–294. https://doi.org/10.1534/genetics.119.302919.
36. Beurton, F., Stempor, P., Caron, M., Appert, A., Dong, Y., Chen, R.A.-J., Cluet, D., Couté, Y., Herbette, M., Huang, N., et al. (2019). Physical and functional interaction between SET1/COMPASS complex component CFP-1 and a Sin3S HDAC complex in C. elegans. Nucleic Acids Res. *47*, 11164–11180. https://doi.org/10.1093/nar/gkz880.
37. Kropp, P.A., Wu, J., Reidy, M., Shrestha, S., Rhodehouse, K., Rogers, P., Sack, M.N., and Golden, A. (2021). Allele-specific mitochondrial stress induced by Multiple Mitochondrial Dysfunctions Syndrome 1 pathogenic mutations modeled in Caenorhabditis elegans. PLoS Genet. *17*, e1009771. https://doi.org/10.1371/journal.pgen.1009771.
38. Westermann, B. (2010). Mitochondrial fusion and fission in cell life and death. Nat. Rev. Mol. Cell Biol. *11*, 872–884. https://doi.org/10.1038/nrm3013.
39. Puccio, H., Simon, D., Cossée, M., Criqui-Filipe, P., Tiziano, F., Melki, J., Hindelang, C., Matyas, R., Rustin, P., and Koenig, M. (2001). Mouse models for Friedreich ataxia exhibit cardiomyopathy, sensory nerve defect and Fe-S enzyme deficiency followed by intramitochondrial iron deposits. Nat. Genet. *27*, 181–186. https://doi.org/10.1038/84818.
40. Schober, F.A., Moore, D., Atanassov, I., Moedas, M.F., Clemente, P., Végvári, Á., Fissi, N.E., Filograna, R., Bucher, A.-L., Hinze, Y., et al. (2021). The one-carbon pool controls mitochondrial energy metabolism via complex I and iron-sulfur clusters. Sci. Adv. *7*, eabf0717. https://doi.org/10.1126/sciadv.abf0717.
41. Schiavi, A., Maglioni, S., Palikaras, K., Shaik, A., Strappazzon, F., Brinkmann, V., Torgovnick, A., Castelein, N., De Henau, S., Braeckman, B.P., et al. (2015). Iron-Starvation-Induced Mitophagy Mediates Lifespan Extension upon Mitochondrial Stress in C. elegans. Curr. Biol. *25*, 1810–1822. https://doi.org/10.1016/j.cub.2015.05.059.
42. Chen, Y., Leboutet, R., Largeau, C., Zentout, S., Lefebvre, C., Delahodde, A., Culetto, E., and Legouis, R. (2021). Autophagy facilitates mitochondrial rebuilding after acute heat stress via a DRP-1–dependent process. J. Cell Biol. *220*, e201909139. https://doi.org/10.1083/jcb.201909139.
43. Al Rawi, S., Louvet-Vallée, S., Djeddi, A., Sachse, M., Culetto, E., Hajjar, C., Boyd, L., Legouis, R., and Galy, V. (2011). Postfertilization Autophagy of Sperm Organelles Prevents Paternal Mitochondrial DNA Transmission. Science *334*, 1144–1147. https://doi.org/10.1126/science.1211878.
44. Wang, Y., Zhang, Y., Chen, L., Liang, Q., Yin, X.-M., Miao, L., Kang, B.-H., and Xue, D. (2016). Kinetics and specificity of paternal mitochondrial elimination in Caenorhabditis elegans. Nat. Commun. *7*, 12569. https://doi.org/10.1038/ncomms12569.
45. Zhou, Q., Li, H., Li, H., Nakagawa, A., Lin, J.L.J., Lee, E.-S., Harry, B.L., Skeen-Gaar, R.R., Suehiro, Y., William, D., et al. (2016). Mitochondrial endonuclease G mediates breakdown of paternal mitochondria upon fertilization. Science *353*, 394–399. https://doi.org/10.1126/science.aaf4777.
46. Labrousse, A.M., Zappaterra, M.D., Rube, D.A., and van der Bliek, A.M. (1999). C. elegans Dynamin-Related Protein DRP-1 Controls Severing of the Mitochondrial Outer Membrane. Mol. Cell *4*, 815–826. https://doi.org/10.1016/S1097-2765(00)80391-3.
47. Roy, C., Molin, L., Alcolei, A., Solyga, M., Bonneau, B., Vachon, C., Bessereau, J.L., and Solari, F. (2022). DAF-2/insulin IGF-1 receptor regulates motility during aging by integrating opposite signaling from muscle and neuronal tissues. Aging Cell *21*, e13660. https://doi.org/10.1111/acel.13660.
48. Regmi, S.G., Rolland, S.G., and Conradt, B. (2014). Age-dependent changes in mitochondrial morphology and volume are not predictors of lifespan. Aging *6*, 118–130. https://doi.org/10.18632/aging.100639.
49. Wei, W., and Ruvkun, G. (2020). Lysosomal activity regulates *Caenorhabditis elegans* mitochondrial dynamics through vitamin B12 metabolism. Proc. Natl. Acad. Sci. USA *117*, 19970–19981. https://doi.org/10.1073/pnas.2008021117.
50. Scholtes, C., Bellemin, S., Martin, E., Carre-Pierrat, M., Mollereau, B., Gieseler, K., and Walter, L. (2018). DRP-1-mediated

apoptosis induces muscle degeneration in dystrophin mutants. Sci. Rep. *8*, 7354. https://doi.org/10.1038/s41598-018-25727-8.

51. Bosch, A., and Calvo, M. (2019). Automated Quantitative Analysis of Mitochondrial Morphology. In Computer Optimized Microscopy Methods in Molecular Biology, E. Rebollo and M. Bosch, eds. (Springer), pp. 99–115. https://doi.org/10.1007/978-1-4939-9686-5_6.
52. Chen, H., and Chan, D.C. (2009). Mitochondrial dynamics-fusion, fission, movement, and mitophagy-in neurodegenerative diseases. Hum. Mol. Genet. *18*, R169–R176. https://doi.org/10.1093/hmg/ddp326.
53. Christian, C.J., and Benian, G.M. (2020). Animal models of sarcopenia. Aging Cell *19*, e13223. https://doi.org/10.1111/acel.13223.
54. Mergoud Dit Lamarche, A., Molin, L., Pierson, L., Mariol, M.-C., Bessereau, J.-L., Gieseler, K., and Solari, F. (2018). UNC-120/SRF independently controls muscle aging and lifespan in Caenorhabditis elegans. Aging Cell *17*, e12713. https://doi.org/10.1111/acel.12713.
55. Liang, V., Ullrich, M., Lam, H., Chew, Y.L., Banister, S., Song, X., Zaw, T., Kassiou, M., Götz, J., and Nicholas, H.R. (2014). Altered proteostasis in aging and heat shock response in C. elegans revealed by analysis of the global and *de novo* synthesized proteome. Cell. Mol. Life Sci. *71*, 3339–3361. https://doi.org/10.1007/s00018-014-1558-7.
56. Etheridge, T., Rahman, M., Gaffney, C.J., Shaw, D., Shephard, F., Magudia, J., Solomon, D.E., Milne, T., Blawzdziewicz, J., Constantin-Teodosiu, D., et al. (2015). The integrin-adhesome is required to maintain muscle structure, mitochondrial ATP production, and movement forces in *Caenorhabditis elegans*. Faseb. J. *29*, 1235–1246. https://doi.org/10.1096/fj.14-259119.
57. Gaffney, C.J., Pollard, A., Barratt, T.F., Constantin-Teodosiu, D., Greenhaff, P.L., and Szewczyk, N.J. (2018). Greater loss of mitochondrial function with ageing is associated with earlier onset of sarcopenia in C. elegans. Aging *10*, 3382–3396. https://doi.org/10.18632/aging.101654.
58. Lin, Y.-F., and Haynes, C.M. (2016). Metabolism and the UPR mt. Mol. Cell *61*, 677–682. https://doi.org/10.1016/j.molcel.2016.02.004.
59. Houtkooper, R.H., Mouchiroud, L., Ryu, D., Moullan, N., Katsyuba, E., Knott, G., Williams, R.W., and Auwerx, J. (2013). Mitonuclear protein imbalance as a conserved longevity mechanism. Nature *497*, 451–457. https://doi.org/10.1038/nature12188.
60. Koopman, M., Michels, H., Dancy, B.M., Kamble, R., Mouchiroud, L., Auwerx, J., Nollen, E.A.A., and Houtkooper, R.H. (2016). A screening-based platform for the assessment of cellular respiration in Caenorhabditis elegans. Nat. Protoc. *11*, 1798–1816. https://doi.org/10.1038/nprot.2016.106.
61. Higashitani, A., Teranishi, M., Nakagawa, Y., Itoh, Y., Sudevan, S., Szewczyk, N.J., Kubota, Y., Abe, T., and Kobayashi, T. (2023). Increased mitochondrial Ca $^{2+}$ contributes to health decline with age and Duchene muscular dystrophy in *C. elegans*. FASEB J *37*, e22851. https://doi.org/10.1096/fj.202201489RR.
62. Huang, S.-H., and Lin, Y.-W. (2018). Bioenergetic Health Assessment of a Single Caenorhabditis elegans from Postembryonic Development to Aging Stages via Monitoring Changes in the Oxygen Consumption Rate within a Microfluidic Device. Sensors *18*, 2453. https://doi.org/10.3390/s18082453.
63. Marchetti, P., Fovez, Q., Germain, N., Khamari, R., and Kluza, J. (2020). Mitochondrial spare respiratory capacity: Mechanisms, regulation, and significance in non-transformed and cancer cells. Faseb. J. *34*, 13106–13124. https://doi.org/10.1096/fj.202000767R.
64. Demine, S., Renard, P., and Arnould, T. (2019). Mitochondrial Uncoupling: A Key Controller of Biological Processes in Physiology and Diseases. Cells *8*, 795. https://doi.org/10.3390/cells8080795.
65. Berry, B.J., Mjelde, E., Carreno, F., Gilham, K., Hanson, E.J., Na, E., and Kaeberlein, M. (2023). Preservation of Mitochondrial Membrane Potential is Necessary for Lifespan Extension from Dietary Restriction. GeroScience *45*, 1573–1581. https://doi.org/10.1007/S11357-023-00766-w.
66. Bertholet, A.M., Chouchani, E.T., Kazak, L., Angelin, A., Fedorenko, A., Long, J.Z., Vidoni, S., Garrity, R., Cho, J., Terada, N., et al. (2019). H+ transport is an integral function of the mitochondrial ADP/ATP carrier. Nature *571*, 515–520. https://doi.org/10.1038/s41586-019-1400-3.
67. Hanover, J.A., Forsythe, M.E., Hennessey, P.T., Brodigan, T.M., Love, D.C., Ashwell, G., and Krause, M. (2005). A Caenorhabditis elegans model of insulin resistance: altered macronutrient storage and dauer formation in an OGT-1 knockout. Proc. Natl. Acad. Sci. USA *102*, 11266–11271. https://doi.org/10.1073/pnas.0408771102.
68. Nielsen, J. (2003). It Is All about MetabolicFluxes. J. Bacteriol. *185*, 7031–7035. https://doi.org/10.1128/JB.185.24.7031-7035.2003.
69. Quirós, P.M., Prado, M.A., Zamboni, N., D'Amico, D., Williams, R.W., Finley, D., Gygi, S.P., and Auwerx, J. (2017). Multi-omics analysis identifies ATF4 as a key regulator of the mitochondrial stress response in mammals. J. Cell Biol. *216*, 2027–2045. https://doi.org/10.1083/jcb.201702058.
70. Locasale, J.W. (2013). Serine, glycine and one-carbon units: cancer metabolism in full circle. Nat. Rev. Cancer *13*, 572–583. https://doi.org/10.1038/nrc3557.
71. Ye, C., Sutter, B.M., Wang, Y., Kuang, Z., and Tu, B.P. (2017). A Metabolic Function for Phospholipid and Histone Methylation. Mol. Cell *66*, 180–193.e8. https://doi.org/10.1016/j.molcel.2017.02.026.
72. Schaeffer, J.M., and Donatelli, M.R. (1990). Characterization of a high-affinity membrane-associated ornithine decarboxylase from the free-living nematode Caenorhabditis elegans. Biochem. J. *270*, 599–604. https://doi.org/10.1042/bj2700599.
73. Leandro, J., and Houten, S.M. (2020). The lysine degradation pathway: Subcellular compartmentalization and enzyme deficiencies. Mol. Genet. Metabol. *131*, 14–22. https://doi.org/10.1016/j.ymgme.2020.07.010.
74. Macrae, M., Plasterk, R.H., and Coffino, P. (1995). The ornithine decarboxylase gene of Caenorhabditis elegans: cloning, mapping and mutagenesis. Genetics *140*, 517–525. https://doi.org/10.1093/genetics/140.2.517.
75. Coffino, P. (2001). Regulation of cellular polyamines by antizyme. Nat. Rev. Mol. Cell Biol. *2*, 188–194. https://doi.org/10.1038/35056508.
76. Jeong, H.D., Kim, J.H., Kwon, G.E., and Lee, S.-T. (2022). Expression of Polyamine Oxidase in Fibroblasts Induces MMP-1 and Decreases the Integrity of Extracellular Matrix. Int. J. Mol. Sci. *23*, 10487. https://doi.org/10.3390/ijms231810487.
77. Park, M.H., Nishimura, K., Zanelli, C.F., and Valentini, S.R. (2010). Functional significance of eIF5A and its hypusine modification in eukaryotes. Amino Acids *38*, 491–500. https://doi.org/10.1007/s00726-009-0408-7.
78. Barnes, V.L., Bhat, A., Unnikrishnan, A., Heydari, A.R., Arking, R., and Pile, L.A. (2014). SIN3 is critical for stress resistance and modulates adult lifespan. Aging *6*, 645–660. https://doi.org/10.18632/aging.100684.
79. Dannenberg, J.-H., David, G., Zhong, S., van der Torre, J., Wong, W.H., and Depinho, R.A. (2005). mSin3A corepressor regulates diverse transcriptional networks governing normal and neoplastic growth and survival. Genes Dev. *19*, 1581–1595. https://doi.org/10.1101/gad.1286905.
80. Baymaz, H.I., Karemaker, I.D., and Vermeulen, M. (2015). Perspective on unraveling the versatility of 'co-repressor' complexes. Biochim. Biophys. Acta *1849*, 1051–1056. https://doi.org/10.1016/j.bbagrm.2015.06.012.
81. van Oevelen, C., Bowman, C., Pellegrino, J., Asp, P., Cheng, J., Parisi, F., Micsinai, M., Kluger, Y., Chu, A., Blais, A., et al. (2010). The Mammalian Sin3 Proteins Are Required for Muscle Development and Sarcomere Specification. Mol. Cell Biol. *30*, 5686–5697. https://doi.org/10.1128/MCB.00975-10.
82. Zhu, F., Zhu, Q., Ye, D., Zhang, Q., Yang, Y., Guo, X., Liu, Z., Jiapaer, Z., Wan, X., Wang, G., et al. (2018). Sin3a–Tet1 interaction activates gene transcription and is required for embryonic stem cell pluripotency. Nucleic Acids Res. *46*, 6026–6040. https://doi.org/10.1093/nar/gky347.
83. Ryan, M.T., and Hoogenraad, N.J. (2007). Mitochondrial-nuclear communications. Annu. Rev. Biochem. *76*, 701–722. https://doi.org/10.1146/annurev.biochem.76.052305.091720.
84. Melber, A., and Haynes, C.M. (2018). UPRmt regulation and output: a stress response mediated by mitochondrial-nuclear communication. Cell Res. *28*, 281–295. https://doi.org/10.1038/cr.2018.16.
85. Shao, L.-W., Peng, Q., Dong, M., Gao, K., Li, Y., Li, Y., Li, C.-Y., and Liu, Y. (2020). Histone deacetylase HDA-1 modulates mitochondrial stress response and longevity. Nat. Commun. *11*, 4639. https://doi.org/10.1038/s41467-020-18501-w.
86. Wai, T., and Langer, T. (2016). Mitochondrial Dynamics and Metabolic Regulation. Trends Endocrinol. Metabol. *27*, 105–117. https://doi.org/10.1016/j.tem.2015.12.001.
87. Vincent, A.E., Ng, Y.S., White, K., Davey, T., Mannella, C., Falkous, G., Feeney, C., Schaefer, A.M., McFarland, R., Gorman, G.S., et al. (2016). The Spectrum of Mitochondrial Ultrastructural Defects in Mitochondrial Myopathy. Sci. Rep. *6*, 30610. https://doi.org/10.1038/srep30610.
88. Byrne, J.J., Soh, M.S., Chandhok, G., Vijayaraghavan, T., Teoh, J.-S., Crawford, S.,

Cobham, A.E., Yapa, N.M.B., Mirth, C.K., and Neumann, B. (2019). Disruption of mitochondrial dynamics affects behaviour and lifespan in Caenorhabditis elegans. Cell. Mol. Life Sci. *76*, 1967–1985. https://doi.org/10.1007/s00018-019-03024-5.

89. Whitnall, M., Suryo Rahmanto, Y., Huang, M.L.-H., Saletta, F., Lok, H.C., Gutiérrez, L., Lázaro, F.J., Fleming, A.J., St Pierre, T.G., Mikhael, M.R., et al. (2012). Identification of nonferritin mitochondrial iron deposits in a mouse model of Friedreich ataxia. Proc. Natl. Acad. Sci. USA *109*, 20590–20595. https://doi.org/10.1073/pnas.1215349109.
90. Ducamp, S., and Fleming, M.D. (2019). The molecular genetics of sideroblastic anemia. Blood *133*, 59–69. https://doi.org/10.1182/blood-2018-08-815951.
91. Ward, D.M., and Cloonan, S.M. (2019). Mitochondrial Iron in Human Health and Disease. Annu. Rev. Physiol. *81*, 453–482. https://doi.org/10.1146/annurev-physiol-020518-114742.
92. de la Cruz-Ruiz, P., Hernando-Rodríguez, B., Pérez-Jiménez, M.M., Rodríguez-Palero, M.J., Martínez-Bueno, M.D., Pla, A., Gatsi, R., and Artal-Sanz, M. (2021). Prohibitin depletion extends lifespan of a TORC2/SGK-1 mutant through autophagy and the mitochondrial UPR. Aging Cell *20*, e13359. https://doi.org/10.1111/acel.13359.
93. Artal-Sanz, M., Tsang, W.Y., Willems, E.M., Grivell, L.A., Lemire, B.D., van der Spek, H., and Nijtmans, L.G.J. (2003). The mitochondrial prohibitin complex is essential for embryonic viability and germline function in Caenorhabditis elegans. J. Biol. Chem. *278*, 32091–32099. https://doi.org/10.1074/jbc.M304877200.
94. Artal-Sanz, M., and Tavernarakis, N. (2009). Prohibitin couples diapause signalling to mitochondrial metabolism during ageing in C. elegans. Nature *461*, 793–797. https://doi.org/10.1038/nature08466.
95. Hernando-Rodríguez, B., and Artal-Sanz, M. (2018). Mitochondrial Quality Control Mechanisms and the PHB (Prohibitin) Complex. Cells *7*, 238. https://doi.org/10.3390/cells7120238.
96. Yoneda, T., Benedetti, C., Urano, F., Clark, S.G., Harding, H.P., and Ron, D. (2004). Compartment-specific perturbation of protein handling activates genes encoding mitochondrial chaperones. J. Cell Sci. *117*, 4055–4066. https://doi.org/10.1242/jcs.01275.
97. Nijtmans, L.G., de Jong, L., Artal Sanz, M., Coates, P.J., Berden, J.A., Back, J.W., Muijsers, A.O., van der Spek, H., and Grivell, L.A. (2000). Prohibitins act as a membrane-bound chaperone for the stabilization of mitochondrial proteins. EMBO J. *19*, 2444–2451. https://doi.org/10.1093/emboj/19.11.2444.
98. Bennett, C.F., Latorre-Muro, P., and Puigserver, P. (2022). Mechanisms of mitochondrial respiratory adaptation. Nat. Rev. Mol. Cell Biol. *23*, 817–835. https://doi.org/10.1038/s41580-022-00506-6.
99. Madeo, F., Eisenberg, T., Pietrocola, F., and Kroemer, G. (2018). Spermidine in health and disease. Science *359*, eaan2788. https://doi.org/10.1126/science.aan2788.
100. Murray Stewart, T., Dunston, T.T., Woster, P.M., and Casero, R.A. (2018). Polyamine catabolism and oxidative damage. J. Biol. Chem. *293*, 18736–18745. https://doi.org/10.1074/jbc.TM118.003337.
101. Pegg, A.E. (2013). Toxicity of Polyamines and Their Metabolic Products. Chem. Res. Toxicol. *26*, 1782–1800. https://doi.org/10.1021/tx400316s.
102. Yang, X., Zhang, M., Dai, Y., Sun, Y., Aman, Y., Xu, Y., Yu, P., Zheng, Y., Yang, J., and Zhu, X. (2020). Spermidine inhibits neurodegeneration and delays aging via the PINK1-PDR1-dependent mitophagy pathway in C. elegans. Aging *12*, 16852–16866. https://doi.org/10.18632/aging.103578.
103. Kumar, V., Mishra, R.K., Ghose, D., Kalita, A., Dhiman, P., Prakash, A., Thakur, N., Mitra, G., Chaudhari, V.D., Arora, A., and Dutta, D. (2022). Free spermidine evokes superoxide radicals that manifest toxicity. Elife *11*, e77704. https://doi.org/10.7554/eLife.77704.
104. Nakanishi, S., and Cleveland, J.L. (2021). Polyamine Homeostasis in Development and Disease. Med. Sci. *9*, 28. https://doi.org/10.3390/medsci9020028.
105. Til, H.P., Falke, H.E., Prinsen, M.K., and Willems, M.I. (1997). Acute and subacute toxicity of tyramine, spermidine, spermine, putrescine and cadaverine in rats. Food Chem. Toxicol. *35*, 337–348. https://doi.org/10.1016/S0278-6915(97)00121-X.
106. Barba-Aliaga, M., and Alepuz, P. (2022). Role of eIF5A in Mitochondrial Function. Int. J. Mol. Sci. *23*, 1284. https://doi.org/10.3390/ijms23031284.
107. Puleston, D.J., Buck, M.D., Klein Geltink, R.I., Kyle, R.L., Caputa, G., O'Sullivan, D., Cameron, A.M., Castoldi, A., Musa, Y., Kabat, A.M., et al. (2019). Polyamines and eIF5A Hypusination Modulate Mitochondrial Respiration and Macrophage Activation. Cell Metabol. *30*, 352–363.e8. https://doi.org/10.1016/j.cmet.2019.05.003.
108. Affronti, H.C., Rowsam, A.M., Pellerite, A.J., Rosario, S.R., Long, M.D., Jacobi, J.J., Bianchi-Smiraglia, A., Boerlin, C.S., Gillard, B.M., Karasik, E., et al. (2020). Pharmacological polyamine catabolism upregulation with methionine salvage pathway inhibition as an effective prostate cancer therapy. Nat. Commun. *11*, 52. https://doi.org/10.1038/s41467-019-13950-4.
109. Kamath, R.S., and Ahringer, J. (2003). Genome-wide RNAi screening in Caenorhabditis elegans. Methods *30*, 313–321.
110. Fan, X., De Henau, S., Feinstein, J., Miller, S.I., Han, B., Frøkjær-Jensen, C., and Griffin, E.E. (2020). SapTrap Assembly of *Caenorhabditis elegans* MosSCI Transgene Vectors. G3 (Bethesda) *10*, 635–644. https://doi.org/10.1534/g3.119.400822.
111. Hoogewijs, D., Houthoofd, K., Matthijssens, F., Vandesompele, J., and Vanfleteren, J.R. (2008). Selection and validation of a set of reliable reference genes for quantitative sod gene expression analysis in C. elegans. BMC Mol. Biol. *9*, 9.
112. Kolotuev, I., Bumbarger, D.J., Labouesse, M., and Schwab, Y. (2012). Targeted Ultramicrotomy. In Methods in Cell Biology (Elsevier), pp. 203–222. https://doi.org/10.1016/B978-0-12-416026-2.00011-X.
113. Li, C.H., and Tam, P.K.S. (1998). An iterative algorithm for minimum cross entropy thresholding. Pattern Recogn. Lett. *19*, 771–776. https://doi.org/10.1016/S0167-8655(98)00057-9.
114. Spanier, B., Laurençon, A., Weiser, A., Pujol, N., Omi, S., Barsch, A., Korf, A., Meyer, S.W., Ewbank, J.J., Palladino, F., et al. (2021). Correction to: Comparison of lipidome profiles of Caenorhabditis elegans—results from an inter-laboratory ring trial. Metabolomics *17*, 33. https://doi.org/10.1007/s11306-021-01784-5.

STAR★METHODS

KEY RESOURCES TABLE

REAGENT or RESOURCE	SOURCE	IDENTIFIER
Antibodies		
IRDye 680RD Goat anti-Mouse IgG	LI-COR Biosciences	Cat# 926-68070, RRID:AB_10956588
Goat anti-Rabbit IgG (H+L) Cross-Adsorbed Secondary Antibody, DyLight™ 800	Thermo Fisher Scientific	Cat# SA5-10036, RRID:AB_2556616
Anti-alpha Tubulin antibody - Microtubule Marker	Abcam	Cat# ab18251, RRID:AB_2210057
Total OXPHOS Rodent WB Antibody Cocktail	Abcam	Cat# ab110413, RRID:AB_2629281
Bacterial and virus strains		
sin-3 (RNAi)	Kamath, R.S. et al.[109]	https://www.dnaform.jp/en/products/clone/c_elegans_rnai_library/I-4K03
mrps-5 (RNAi)	Kamath, R.S. et al.[109]	https://www.dnaform.jp/en/products/clone/c_elegans_rnai_library/V-8K16
nuo-4 (RNAi)	Kamath, R.S. et al.[109]	https://www.dnaform.jp/en/products/clone/c_elegans_rnai_library/III-3F02
E. coli OP50	CGC	WB Cat# WBStrain00041969
E. coli RNAi feeding strain L4440 HT115(DE3)	source bioscience	WB Cat# WBStrain0004107
Chemicals, peptides, and recombinant proteins		
Tetramethylrhodamine, ethyl ester, perchlorate (TMRE)	Invitrogen™	Cat# T669
MitoTracker™ Dyes for Mitochondria Labeling	Invitrogen™	Cat# M7512
formvar coated grid, stabilized with evaporated carbon film	Electron Microscopy Science	Cat# FCF2010-Cu
Carbonyl cyanide 4-(trifluoromethoxy) phenylhydrazone (FCCP)	Sigma-Aldrich	Cat#C2920 CAS : 370-86-5
Sodium azide	Sigma-Aldrich	Cat#13412 CAS: 26628-22-8
Deposited data		
Raw transcriptomics data	Caron et al.[34]	GEO : GSE227499
Raw metabolomics files	This paper	https://www.ebi.ac.uk/metabolights/index: MTBLS8439
Experimental models: Organisms/strains		
C. elegans: Strain N2 Bristol	Caenorhabditis Genetics Center	RRID:WB-STRAIN:WBStrain00000001
C. elegans: Strain SJ4100 *zcIs13[hsp-6p::GFP+lin-15(+)]*	Caenorhabditis Genetics Center	RRID:WB-STRAIN:WBStrain00034068
C. elegans: Strain PFR590 *sin-3(tm1276)I*	Beurton et al.[36]	N/A
C. elegans: Strain PHX2172 *sin-3(syb2172)/hT2[bli-4(e937)let-?(q782)qIs48]I*	Caron et al.[34]	N/A
C. elegans: Strain EN7714 *krSi134[myo-3p::tomm-20Nter::wrmScarlet]*	Roy et al.,[47]	N/A
C. elegans: Strain EGD629 *eagxSi155[mex-5p::tomm-20::mKate2::pie-13'UTR+unc-119(+)]II*	Fan X, et al.[110]	N/A
C. elegans: Strain KAG420 *kagIs4[gfp::myo-3]V*	Mergoud Dit Lamarche et al.[54]	N/A

(*Continued on next page*)

Continued

REAGENT or RESOURCE	SOURCE	IDENTIFIER
C. elegans: Strain PFR750 *sin-3(tm1276)I;kagIs4[gfp::myo-3]V*	This study	N/A
C. elegans: Strain PFR754 *sin-3(tm1276)I;krSi134[myo-3p::tomm-20Nter::wrmScarlet]*	This study	N/A
C. elegans: Strain PFR758 *sin-3(tm1276);egxSi155[mex-5p::tomm-20::mKate2::pie-13'UTR+unc-119(+)]II*	This study	N/A
C. elegans: Strain PFR669 *sin-3::mCherry(syb521);oxIs279[pie-1p::GFP::H2B+unc-119(+)]II*	This study	N/A
Oligonucleotides		
sin-3_for:AGGGCCAACAGTCAACAACA	This study	N/A
sin-3_rev:GACGATGATGGGCCAGGATT	This study	N/A
mrps-5_for:CAACTGGCCGAACGAAAAGG	This study	N/A
mrps-5_rev:CTCGGTCTTGAGTTCAGTGGA	This study	N/A
nuo-4_for:GGACACCATCTTCCAGAACCA	This study	N/A
nuo-4_rev:TCCGAATCCAAATCCAGCGA	This study	N/A
act-1_for:gctggacgtgatcttactgattacc	Hoogewijs D et al.[111]	N/A
act-1_rev:gtagcagagcttctccttgatgtc	Hoogewijs D et al.[111]	N/A
cdc-42_for:ctgctggacaggaagattacg	Hoogewijs D et al.[111]	N/A
cdc-42_rev:ctcggacattctcgaatgaag	Hoogewijs D et al.[111]	N/A
Software and algorithms		
ImageJ	https://imagej.net/	ImageJ (RRID:SCR_003070)
GraphPad Prism	http://www.graphpad.com/	GraphPad Prism (RRID:SCR_002798)
viridis	https://cran.r-project.org/web/packages/viridis/vignettes/intro-to-viridis.html	viridis (RRID:SCR_016696)
ggsignif	https://cran.r-project.org/package=ggsignif	ggsignif (RRID:SCR_023047)
readxl	https://cran.r-project.org/web/packages/readxl/index.html	readxl (RRID:SCR_018083)
scales	https://CRAN.R-project.org/package=scales	scales (RRID:SCR_019295)

RESOURCE AVAILABILITY

Lead contact

Further information and requests for resources and reagents should be directed to and will be fulfilled by the lead contact, Francesca Palladino (francesca.palladino@ens-lyon.fr).

Materials availability

C. elegans strains generated in this study are available upon request.

Data and code availability

- Metabolomics data have been deposited at MetaboLights with the study ID MTBLS8439 and are publicly available as of the date of publication. Accession numbers are listed in the key resources table. Raw transcriptomics data were deposited in GEO with accession number GSE227499 (Caron et al.[34]). Microscopy data reported in this paper will be shared by the lead contact upon request.
- This paper does not report original code
- Any additional information required to reanalyze the data reported in this paper is available from the lead contact upon request.

EXPERIMENTAL MODEL AND STUDY PARTICIPANT DETAILS

C. elegans strains were cultured on Nematode Growth Medium (NGM) agarose plates with Escherichia coli OP50 and incubated at 20°C. The following strains were used: wild type N2 Bristol, PFR590 *sin-3(tm1276)*I, PHX2172 *sin-3(syb2172)*/hT2[*bli-4(e937)let-?(q782)qIs48*]I, KAG420 *kagIs4*[*gfp*::*myo-3*]V, PFR750 *sin-3(tm1276)*I;*kagIs4*[*gfp*::*myo-3*]V, EN7714 *krSi134*[*myo-3p*::*tomm-20Nter*::wrmScarlet], PFR754 *sin-3(tm1276)*I;*krSi134*, EGD629 *egxSi155*[*mex-5p*::*tomm-20*::mKate2::*pie-1* 3'UTR + *unc-119*(+)]II, PFR758 *sin-3(tm1276)*; *egxSi155*, PFR669 *sin-3*::mCherry(*syb521*); *oxIs279*[*pie-1p*::GFP::H2B + *unc-119*(+)]II; SJ4100 *zcIs13*[*hsp-6p*::GFP+*lin-15(+)*]. PFR750 and PFR754 were obtained by crossing *sin-3(tm1276)* hermaphrodites with GFP::*myo-3* or *myo-3p*::*tomm-2*0Nter::wrmScarlet males, respectively.

METHOD DETAILS

Gene enrichment analysis

Enrichment analysis was carried out using WormCat (http://wormcat.com/), a nematode-specific gene ontology enrichment analysis and visualisation tool allowing for analysis of specific pathways. For DEGs functional analysis, significantly up- and downregulated genes were input to WormCat[35] using default settings. Significance scores are reported as Fisher's exact test P-values.

Transmission electron microscopy

Worms (young adults) were fixed by HPF with EMPACT-2 (Leica Microsystems) and then freeze substituted in anhydrous acetone containing 1% OsO4, 0.5% glutaraldehyde and 0.25% uranyl acetate for 60 h in a FS system (AFS-2, Leica Microsystems). Larvae were embedded in Epon-Araldite mix (EMS hard formula). To gain better anteroposterior orientation and sectioning, adhesive frames were used (11560294 GENE-FRAME 65 μl, Thermo Fisher Scientific) for flat-embedding, as previously described.[112] Ultrathin sections were cut on an ultramicrotome (UC7; Leica Microsystems) and collected on formvar-coated slot grids (FCF2010-CU, EMS). Each larva was sectioned in five different places with ≥ 10 μm between each grid to ensure that different cells were observed. Each grid contained at least 5-10 consecutive sections of 70 nm. TEM grids were observed using a JEM-1400 transmission electron microscope (JEOL) operated at 120 kV, equipped with a Gatan Orius SC200 camera (Gatan) and piloted by the Digital Micrograph program. To quantify mitochondria, we used Image J. The clearly discernible outlines of the mitochondria were traced with the magic wand tool and the number of mitochondria was counted; the surface area (size of the mitochondria) is expressed in square micrometers; the perimeter in micrometers. Circularity [$4\pi\cdot$(area/perimeter 2)] is an index with values of 1 indicating perfect spheroids.

Quantification of muscle mitochondria and imaging of myofilament structure

For mitochondria and myofilament observation in muscle cells, staged worms at the young adult stage were mounted on agarose pads in M9 solution containing 10% sodium azide. Muscles in the posterior part of worms were imaged. Z-stack images were acquired using a Zeiss LSM980 inverted confocal microscope with 63× oil immersion objective. Z-stacks were acquired every 0.27μm to image mitochondria and every 0.23μm to image myofilaments. Images shown are projections using max intensity method in Fiji. Manual quantification of mitochondrial morphology in body wall muscle cells was performed in double blind experiments according to the following criteria: cells containing long interconnected mitochondrial networks were classified as tubular, cells containing a combination of interconnected mitochondrial networks along with smaller fragmented mitochondria were classified as intermediate, and cells with sparse small round mitochondria were classified as fragmented.[48] Automated quantification was based on Boch and Calvo (2019), following conversion of raw images to binary images using ImageJ. Briefly, maximum projection was applied to z-stacks. To correct for heterogeneous background, a median filter (kernel radius=20) was subtracted. To remove salt and pepper noise after subtraction, a median filter (kernel radius=1) was applied to the resulting image. Finally, images were binarised using the auto threshold Li's method.[113] The "analyze particles filter" (size=1-Infinity; exclude on edges) was used prior quantification.

TMRE and Mitotracker staining

Mitochondrial membrane potential was measured using the tetramethylrhodamine ethyl ester dye (TMRE, Invitrogen) and mitochondrial content was measured using Mitotracker Green FM (MTG, Invitrogen). Synchronized animals were grown at 20°C until the appropriate stage (day 5 adulthood) and then transferred to NGM plates in the presence of the dye (2,5 μM TMRE or 100 nm MTG) for 17 h. Next, for intestinal clearing and prior to imaging, worms were transferred 1h to NGM plates without dye. Animals were then mounted on 2% agarose pads with 10 mM Levamisole and imaged using an ORCA-Flash4.0 LT Hamamatsu digital camera on a Leica M205 Stereoscope equipped with a Plan Apo 5.0x/0.50 LWD (TMRE) or Plan Apo 1x (MTG) objective. Segmentation of the head (TMRE) or the whole worm (MTG) was done with the free hand tool from ImageJ software. Emission intensity was measured on greyscale images with a pixel depth of 16 bits. Aged worms with internal organ extrusion through the vulva were censored. At least two independent assays (11-31 worms each) were performed and the combined data was analyzed using theGraphPad Prism software.

Activation of UPRmt by RNAi treatment

RNAi bacteria were induced by directly adding 1 mM IPTG directly onto the bacteria lawn 2 hours before the transfer of worms 112. Transgenic animals expressing *hsp-6*::GFP were synchronized by bleaching, and the L1 stage animals obtained transferred to empty vector HT115 or *sin-3*(RNAi) 35mm plates, and allowed to develop to egg-laying adults (P0). 4-6 P0 adults from each RNAi treatment were then individually transferred onto: 1) empty vector control; 2) single RNAi (*sin-3*, *nuo-4*, *mrps-5*) or double RNAi plates (*sin-3/nuo-4*, *sin-3/mrps-5*) to induce mitochondrial stress in F1 progeny. *sin-3* RNAi treatment was started in P0 animals to ensure depletion of maternal SIN-3 protein in scored animals. GFP expression was assessed in F1 progeny 5 days after egg lay. For imaging, worms were immobilized using 2.5mM Levamisole in M9 buffer (22mM KH_2PO_4, 42mM Na_2HPO_4, 86mM NaCl, 1mM $MgSO_4$). Images were acquired with a Nikon AZ100M microscope.

Oxygen consumption measurements

Worm oxygen consumption was measured using the Agilent Seahorse XFp Analyzer. Animals were synchronized by allowing gravid mothers to lay eggs for 2-3 hours before removing them from plate. Worms (20-30 per well) at the young adult stage or at day 6 of adulthood were transferred into M9-filled Seahorse plates. Working solutions were diluted in M9 at the following final concentrations: Carbonyl cyanide 4-(trifluoromethoxy) phenylhydrazone (FCCP) (Sigma-Aldrich) 250 μM, NaN_3 (Sigma-Aldrich) 400 mM. Oxygen Consumption Rate (OCR) measurements were repeated 8 times in basal conditions, 10 times after FCPP injection (for maximal respiration), and 4 times after NaN_3 injection (no mitochondrial respiration). Each cycle consisted of 3 min mix, 30 second wait, and 3 min measure. Values were normalized per worm. Three independent assays were carried out and the combined data was analyzed by Unpaired t-test, or, when appropriate, Mann-Whitney test, using GraphPad Prism software.

Western blot analysis

Young adult worms were collected in M9 buffer, washed 3 times, pelleted and frozen in dry ice. Pellets were resuspended in TNET buffer (50 mM Tris·HCl (pH 8), 300 mM NaCl, 1 mM EDTA, 0,5% Triton X-100 and cOmplete™ Protease Inhibitor Cocktail [Merck # 11697498001]) and lysed with zirconium beads [Lysing Matrix Y, MP Biomedicals #116960050] using a Precellys24 homogenizer [Ozyme] with the following parameters: 6000 rpm 2x20sec. Homogenates were centrifuged and supernatants aliquoted and frozen at −80°C. Total protein amount was quantified by the Bradford assay [Bio-Rad]. 10,20,30,40,50 and 80 ug of protein extracts were loaded either on 12% NuPage Novex or 12 % SDS PAGE gels for western blot analysis. After transfer, membranes were incubated overnight with total OXPHOS Rodent WB Antibody Cocktail [Abcam #ab110413] diluted at 1:500 or anti-alpha-tubulin [Abcam #ab18251] diluted at 1:5,000. The next day, membranes were incubated for 1 hour with goat anti-rabbit DyLight™ 800 [Invitrogen # SA5-10036] and IRDye® 680RD goat anti-mouse [LiCOR #926-68070] diluted at 1:10,000. Aquisition was performed on a ChemiDoc MP apparatus [Bio-Rad]. Quantification was carried out using Image J, and each protein signal was normalized to the level of tubulin. Two to three independent biological replicates and three to four technical replicates were used for quantification.

Metabolite extraction and profiling

Embryos derived from bleaching were transferred onto 90 mm plates seeded with 0P50 bacteria and left to develop to the young adult stage. Animals were collected in M9 medium, washed 3 times in 10 ml M9, and pellets quick frozen in liquid nitrogen[114] prior to processing. 8 replicas, each containing approximately 2000 worms, were processed per genotype. All chemicals and solvents were of LC-MS or analytical grade. *C. elegans* samples were thawed on ice and 1 ml of ice-cold $H_2O/MeOH/CHCl_3$ (1/3/1, v/v/v). After suspension in solvent, samples were transferred to 2 ml MN Bead Tubes Type A (Macherey-Nagel, Düren, Germany) and lysed using a Precellys Bead Beating system with an additional Cryolys cooling module (Bertin Instruments, Montigny-le-Bretonneux, France). After lysis, samples were incubated for 10 minutes in an ice-cold ultrasonic bath, followed by centrifugation at 4°C and 13,000 rpm for 15 minutes. The supernatant was transferred to a fresh reaction tube and evaporated to dryness using a centrifugal evaporator. Proteins were extracted from residue debris pellets and quantified using a BCA kit (Sigma-Aldrich, Taufkirchen, Germany). Metabolite profiling was performed using a Sciex ExionLC AD coupled to a Sciex ZenoTOF 7600 under the control of Sciex OS 3.0 (Sciex, Darmstadt, Germany). Separation was achieved on an Agilent InfinityLab Poroshell 120 HILIC-Z column (2.1 mm x 150 mm, 2.7 μm particle size, PEEK-lined) (Agilent Technologies, Waldbronn, Germany). Different eluents and gradients were applied for positive and negative ionization modes. In positive ionization mode, eluent A consisted of 100% H_2O + 10 mM ammonium formate / 0.1% formic acid, and eluent B consisted of 10% H_2O / 90% ACN + 10 mM ammonium formate / 0.1% formic acid. In negative ionization mode, eluent A consisted of 100% H_2O + 10 mM ammonium acetate / 2.5 μM medronic acid, pH = 9, and eluent A consisted of 15% H_2O / 85% ACN + 10 mm ammonium acetate / 2.5 μM medronic acid, pH = 9. The column temperature was set to 25°C and 50°C for positive and negative ionization modes, respectively, and the flow rate was 0.25 mL/min in both cases. Gradients for both ionization modes are summarized in Table S3. Dried samples were re-dissolved in 50 μL H_2O/ACN (1/3, v/v), and 40 μL were transferred to an autosampler vial and 10 μL to a pooled QC sample. Autosampler temperature was set to 5°C and 5 μl were injected for analysis. In MS1, ions in the m/z range 70 to 1500 were accumulated for 0.1s, and information-dependent acquisition (IDA) of MS2 was used with a maximum number of 6 candidate ions and a collision energy of 35 eV with a spread of 15 eV. Accumulation time for MS2 was set to 0.025 seconds, yielding a total cycle time of 0.299 seconds. ZenoTrapping was enabled with a value of 80000. QC samples were used for conditioning the column and were injected every ten samples. Automatic calibration of the mass spectrometer in MS1 and MS2 mode was performed every five injections using the ESI positive Calibration Solution for the Sciex X500 system or the ESI negative Calibration Solution for the Sciex X500 system (Sciex, Darmstadt, Germany).

Metabolite data analysis

Data analysis was performed in a targeted fashion for identified metabolites (see Tables S4 and S5). Metabolites were identified by comparison to in-house reference standards, publicly available reference spectra, and manual interpretation of fragmentation spectra. Data analysis was performed in Sciex OS 3.0.0.3339 (Sciex, Darmstadt, Germany). Peaks for all metabolites indicated in Tables S4 and S5 were integrated with an XIC width of 0.02 Da and a Gaussian smooth width of 3 points using the MQ4 peak-picking algorithm. Peak areas were exported to a .txt file and normalized according to the protein content of the respective sample. All further processing was performed in R 4.2.1 within RStudio using the following packages: tidyverse (1.3.2), readxl (1.4.1), ggsignif (0.6.4), gghalves (0.1.4), scales (1.2.1) and viridis (0.6.2). Data were plotted using ggplot with gghalves using half box- and half dot-plots. Significance was tested using a Welch test within ggsignif.

QUANTIFICATION AND STATISTICAL ANALYSIS

Details of all quantification methods and statistical analyses used in this paper are reported in the relevant STAR Methods sections and figure legends, and summarized hereafter. Figure 1: Significance scores are reported as Fisher's exact test p-value; Figure 2: at least 2-3 mitochondria on 25 to 60 images per condition scored; Figure 3: total number of worms scored for each condition is indicated above bars, measured parameters are average perimeter, average area and average roundness (as specified in material and methods, 12-15 animals per condition), data represents mean ± SD calculated using unpaired t test or Mann Whitney test. Quantification of Mitotracker Green and TMRE staining represent the mean ± SD of 2-3 independent replicates, where each data point represents one worm and Statistical differences were calculated using Mann Whitney test; Figure 4: data is representative of one of two independent experiments with 30 animals per condition each, repeated 8 times in basal conditions, 10 times after FCPP injection, and 4 times after NaN3 injection, with three independent assays carried out and the combined data analyzed by Unpaired t-test, or, when appropriate, Mann-Whitney test, using GraphPad Prism software. For western blot levels of each protein were quantified with Image J. Bar plot represents the mean of two to three independent biological replicates; error bars correspond to SD; Figure 6: p-value calculated using a Welch test. All softwares used for quantification and statistical analysis are reported in the Method details and in the key resources table.